Effect of Induced Wheel and Impeller Inlet Diameter on the Hydrodynamic Performance of High-speed Centrifugal Pumps

Y. Long [1†], H. Wang[1], R. Wang [1], B. He [2], Q. Fu [1] and R. Zhu [1]

[1] National Research Center of Pumps, Jiangsu University, Zhenjiang 212013, China
[2] Shaanxi Wofeng Fluid Technology Co., Ltd, Xi'an 710199, China

†Corresponding Author Email: longyun@ujs.edu.cn

ABSTRACT

The high-speed centrifugal pump plays a crucial role in fields such as aerospace and petrochemical industries, owing to its characteristics of elevated rotational speed and high head. During high-speed operation, the centrifugal pump is prone to cavitation, which alters the fluid flow state within the pump, leading to vibrations, noise, and a sudden decrease in pump head and efficiency. Simultaneously, the collapse of cavitation bubbles generates impact pressure that can damage the pump's internal flow components, significantly reducing its operational lifespan and causing severe consequences. Moreover, under constant-flow conditions, the absolute and relative velocities of the fluid at the impeller inlet are functions of the suction pipe diameter. Therefore, there exists an optimal value for the impeller inlet diameter to enhance the centrifugal pump's resistance to cavitation. Similarly, the different geometric and structural parameters of the inducer also influence the hydraulic performance of the centrifugal pump. The focus of this study is on the external characteristics and internal flow patterns of an optimized high-speed centrifugal pump. In this paper, the entire flow field of the model pump is numerically simulated using ANSYS CFX software. The performance and overall flow field state of the high-speed centrifugal pump under different impeller configurations and inlet diameters are explored. The influence of blade wrap angle and inlet diameter on the high-speed centrifugal pump is revealed, providing a theoretical basis for subsequent optimal design.

1. INTRODUCTION

Owing to its numerous advantages, including low flow rates, high lift capabilities, and reliable performance, the high-speed centrifugal pump has found widespread applications across diverse sectors such as high-rise building firefighting, the chemical industry, water conservancy, and aerospace. With the rapid economic growth in our country, the demand for centrifugal pumps is on a constant rise, and concurrently, the operational stability and performance requirements for pumps have escalated to an even higher level.

Currently, industries such as aerospace and chemical engineering are experiencing rapid growth. To reduce the weight of engines and oil-related equipment, it is necessary to elevate the pump's installation position. Therefore, to achieve the desired outcome of a low flow rate and high head in the design of high-speed centrifugal pumps, it is imperative to employ specialized design techniques and elevate the rotational speed of the impeller. Additionally, the employment of low-specific-speed compound impellers has been instrumental in addressing this challenge. Given the diverse and extreme operating conditions encountered, the operational safety and stability of centrifugal pumps have garnered significant attention. Acknowledging the inevitability occurrence of cavitation during high-speed operation, it is imperative to recognize cavitation as a crucial determinant of the stable performance of centrifugal pumps (Zhao, 2021a; Tong, 2020).

Driven by the global demands for energy conservation, environmental protection, and carbon reduction, the independent design and development of high-performance centrifugal pumps have become an urgent task. Currently, the design of the inducer impeller mainly relies on empirical formulas and demands a high level of design experience. However, with the increasing extremity of operating environments, the requirements for the performance of the inducer impeller and the pump itself become more stringent. Consequently, optimizing the geometric parameters to improve the cavitation performance of the inducer impeller has become a popular research topic. Furthermore, considering the interaction between the inducer impeller and the main impeller, optimizing the geometric parameters of the main impeller is particularly important to ensure more stable inlet conditions. Therefore, the exploration of optimization design methods for the inducer impeller and the main impeller serves as a theoretical basis for the subsequent development, design, and application of high-performance centrifugal pumps.

Numerous researchers have explored the flow characteristics within centrifugal pumps through experimental measurements and numerical simulations. Wang et al. elucidated the attributes of the unsteady flow phenomenon occurring within the impeller of a centrifugal pump amidst cavitation conditions. Their experiments demonstrated that cavitation at the equilibrium hole was less likely to diffuse and transfer, the emergence of cavitation has exerted a substantial influence on the pressure experienced by the blades located at the back side of the impeller (Wang et al., 2020). Wang used the computational fluid dynamics method. Several monitoring points were set on the volute to analyze the changes in pressure pulsation and radial force as the impeller rotates at different angles. found out that the pressure pulsation in the single-channel pump volute is induced by the rotor-stator interaction and its harmonics. The monitoring points close to the separation tongue along the rotation direction of the impeller are more affected by the flow rate (Wang et al., 2023). Yu considered the effect of impeller eccentricity caused by parallel misalignment of the coupling, and the impact of the impeller eccentricity on the hydrodynamic characteristics of a centrifugal pump is numerically investigated. He found out that the eccentric impeller will deteriorate the hydraulic performance of the pump, nonetheless the influence is limited. However, it significantly affects the amplitude of the flow-induced force at shaft frequency, and the amplitude is proportional to the eccentricity ratio to some extent. The influence of impeller eccentricity on pressure pulsation can be evaluated by the shaft orbit. The crest factor of the impeller trajectory is positively correlated with the pressure pulsation intensity (Yu et al., 2023). Yang used numerical simulations to show the significant increase in pressure fluctuation amplitude at the tongue region under cavitation conditions (Yang et al., 2020).

To assess the degree of cavitation and improve the cavitation performance of pumps, experts and scholars have also conducted research. Jure analyzed the vibration and noise signals generated during the cavitation process of centrifugal pumps and proposed a method to judge the degree of cavitation (Murovec et al., 2020). Song optimized the pre-cavitation suppression device of the inducer by changing the forward and backward tilt angles of the guide vane. They focused on studying the influence of the forward tilt angle on pressure and reversed flow velocity and analyzed cavitation inside a high-speed centrifugal pump to determine the optimal solution (Song et al., 2020). Cui proposed a jetting fluid device to improve the cavitation performance of centrifugal pumps (Cui et al., 2019).

The structure and parameters of the impeller have a significant impact on the cavitation performance of centrifugal pumps, and scholars from both domestic and international platforms have conducted extensive research on this matter. Al Obaidi employed computational fluid dynamics (CFD) simulations to investigate the internal flow field of a centrifugal pump with different outlet impeller diameters under single-phase and cavitation conditions. The study examined the variation in pump speed and static pressure across a range of different outlet impeller diameters. Reliable models were established and validated for various pump operating conditions, and an analysis of the temporal and spectral characteristics of pressure fluctuations was conducted (Al-Obaidi et al., 2022). Zhang found that opening holes at the blade inlet can effectively suppress cavitation inside centrifugal pumps (Zhang et al., 2021). Zhao proposed setting roughened strips at the leading edge of the suction side of the impeller to improve the cavitation performance of centrifugal pumps (Zhao et al., 2021b). Their research showed that setting roughened strips optimized the flow field distribution and had some inhibitory effect on the development of cavitation bubbles at the incipient stage, thus effectively improving the cavitation performance of centrifugal pumps. Furthermore, Zhao investigated the influence of three different obstacles placed at the impeller blade outlet, as shown in Fig. 2, on the cavitation performance of centrifugal pumps. They concluded that

Fig. 1. Blade surface subjected to cavitation erosion

Fig. 2 Blade model with the three structures

Table 1 Main geometric parameters of impeller

Inlet Diameter D_2/Mm	Outlet Diameter D_2/Mm	Outlet Width b_2/Mm	Blade Inlet Angle β_1/°	Blade Outlet Angle β_2/°	Vane Wrap Angle φ_2/°	Blade Number Z
90	145	14	14.2	20	110	5

Table 2 Main geometric parameters of inducer

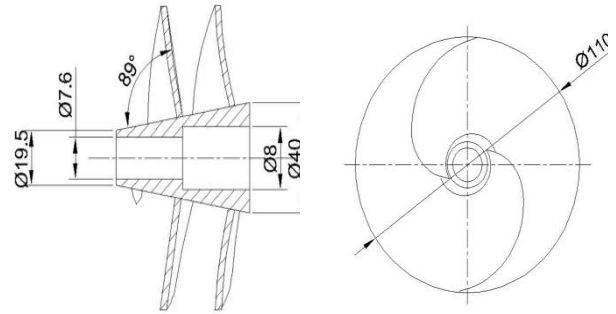| Geometric Parameter	Size
Rim Diameter D_y/mm	110
Wheel Inlet Diameter d_{h1}/mm	19.5
Wheel Outlet Diameter d_{h2}/mm	40
Rim Inlet Blade Angle β_{y1}/°	7.6
Rim Outlet Blade Angle β_{y2}/°	8.0
Blade Wrap Angle φ /°	260
Blade Swept-back Angle $\Delta\varphi$ /°	100

the performance of cavitation in centrifugal pumps is best when the obstacles are arranged transversely (Zhao et al., 2022).

In conclusion, scholars from both domestic and international platforms have combined experimental measurements and numerical calculations to explore the flow characteristics and pressure pulsation characteristics

of cavitation inside centrifugal pumps. They have also proposed methods to improve the cavitation performance of centrifugal pumps starting from the geometric parameters and structure of the impeller. This provides valuable insights for the numerical simulations and research approach in this paper. Building upon this foundation, this paper will further investigate the flow and cavitation performance inside high-speed centrifugal pumps under a full-flow field condition.

2. PHYSICAL MODEL AND NUMERICAL CALCULATION METHOD

2.1 Geometric Models

The selected high-speed pump exhibits a rated flow rate of 338.1 m3/h, a designed head of 1052 m. and a rated speed of 20000 r/min. The primary geometric parameters of the impeller are presented in Table 1, while those of the inducer are presented in Table 2.

Fig. 3 The Structure of inducer wheel

Figure 3 shows the structure of inducer wheel, some dimensions have been marked in the diagram. The definition of the blade inlet and outlet placement angle pertains to the geometric relationship between the tangents of the blade's inlet and outlet edges, respectively, and the tangent of the intersection point where the impeller's outer circumference meets. Furthermore, the blade sweep angle, which characterizes the aerodynamic configuration of a wind turbine blade, is defined as the angle formed between the trailing edge line and the leading edge line of the blade. These definitions provide crucial insights into the design and performance analysis of blades, enabling engineers and researchers to accurately assess and optimize their aerodynamic properties.

2.2 Numerical Computation Theory

2.2.1 Governing Equation

In the research and calculation process of this paper, the fluid medium is assumed to be incompressible and viscous, similar to clear water. The study assumes a constant temperature environment, neglecting heat exchange and the impact of heat transfer in the flow field. The control equations are as follows:

(1) Continuity equation

The mathematical expression of the continuity equation in the right-angled coordinate system is shown below :

$$\frac{\partial(u)}{\partial x} + \frac{\partial(v)}{\partial y} + \frac{\partial(w)}{\partial z} = 0 \tag{1}$$

In this equation, u represents the velocity component in the x direction of the fluid; v represents the velocity component in the y direction of the fluid; wrepresents the velocity component in the z direction of the fluid.

(2) Conservation of momentum equation

The mathematical expression for the conservation of momentum equation is shown below:

$$\rho\left(\frac{\partial u}{\partial t} + u\frac{\partial u}{\partial x} + v\frac{\partial u}{\partial y} + w\frac{\partial u}{\partial z}\right) = -\frac{\partial p}{\partial x} + \mu\left(\frac{\partial \tau_{xx}}{\partial x} + \frac{\partial \tau_{yx}}{\partial y} + \frac{\partial \tau_{zx}}{\partial z}\right) + \rho F_x \tag{2}$$

$$\rho\left(\frac{\partial v}{\partial t} + u\frac{\partial v}{\partial x} + v\frac{\partial v}{\partial y} + w\frac{\partial v}{\partial z}\right) = -\frac{\partial p}{\partial y} + \mu\left(\frac{\partial \tau_{xy}}{\partial x} + \frac{\partial \tau_{yy}}{\partial y} + \frac{\partial \tau_{zy}}{\partial z}\right) + \rho F_y \tag{3}$$

$$\rho\left(\frac{\partial w}{\partial t} + u\frac{\partial w}{\partial x} + v\frac{\partial w}{\partial y} + w\frac{\partial w}{\partial z}\right) = -\frac{\partial p}{\partial z} + \mu\left(\frac{\partial \tau_{xz}}{\partial x} + \frac{\partial \tau_{yz}}{\partial y} + \frac{\partial \tau_{zz}}{\partial z}\right) + \rho F_z \tag{4}$$

In this equation, μ is the kinetic viscosity; τ_{xx}、 τ_{yy}、 τ_{zz} are the viscous force components; F_x、 F_y、 F_z are the volumetric force components.

2. 2. 2 Governing Equation

For laminar flow, the N-S equations are sufficient for resolution. However, in practical engineering scenarios, fluid flow is predominantly turbulent, which represents a complex flow phenomenon commonly encountered in such applications. The N-S equations do not fully capture the intricacies of turbulent fluid flow during computational analysis. In turbulent flow conditions, it is acceptable to disregard the details of fluctuations and instead perform suitable averaging of the N-S equations. The resulting averaged flow equations, along with the accompanying mathematical formulas, form the basis of a turbulent model.

An accurate and reliable turbulent model plays a crucial role in simulation calculations for hydraulic machinery. In current engineering applications, the widely used two-equation turbulent models encompass the standard k-ε model, RNG k-ε model, realizable k-ε model, among others, as well as SST k-ω model. The SST k-ω model, which combines the benefits of the standard k-ε model for far-field calculations and the k-ω model for near-wall zone computations, boast a wide application scope and computational results that closely align with experimental outcomes. Therefore, this study employs the SST k-ω model for calculations. Based on careful consideration. First proposed by Menter, the SST k-ω model's mathematical expression is presented below."

$$\frac{\partial(\rho k)}{\partial t} + \frac{\partial(\rho k u_i)}{\partial x_i} = \frac{\partial}{\partial x_j}\left[\left(\mu + \frac{\mu_t}{\sigma_{k3}}\right)\frac{\partial k}{\partial x_j}\right] + G_k - Y_k + S_k \tag{5}$$

$$\frac{\partial(\rho \omega)}{\partial t} + \frac{\partial(\rho \omega u_i)}{\partial x_i} = \frac{\partial}{\partial x_j}\left[\left(\mu + \frac{\mu_t}{\sigma_{\omega 3}}\right)\frac{\partial \omega}{\partial x_j}\right] + G_\omega - Y_\omega + D_\omega + S_\omega \tag{6}$$

In this equation, ρ represents the fluid density; k is the turbulent kinetic energy; ω is the specific dissipation rate; uj is the velocity component; μ is the molecular viscosity; μ_t is the turbulent viscosity; G_k and G_ω are the production terms of turbulent kinetic energy and specific dissipation rate due to mean velocity gradients and turbulent velocity gradients; Y_k and Y_ω are the dissipation terms of turbulent kinetic energy and specific dissipation rate; D_ω is the cross-diffusion term, which considers the interaction between turbulent kinetic energy and specific dissipation rate; S_k and S_ω are the defined source terms; σ_k and σ_ω are the reciprocal of the effective Prandtl numbers for turbulent kinetic energy and specific dissipation rate, respectively.

2.3 Numerical Calculation Method

2. 3. 1 Computational Model

The flow-passing parts of the high-speed centrifugal pump are modeled based on the design parameters outline in section 2.2.

To ensure sufficient flow development, and stability, as well as to facilitate the analysis of internal flow patterns within the inlet section, the length of the inlet and outlet extensions is set to four times the diameter of the pipe.

The lengths of inlet and outlet extensions play a pivotal role in fluid systems, crucial for maintaining stable flow conditions as fluids enter and exit pipelines or equipment. By optimizing these extension lengths, we can significantly reduce energy losses in the transition regions and enhance the accuracy of measurement parameters, both of which are crucial for assessing and optimizing the performance of fluid systems. Currently, the selection of extension lengths is primarily based on fundamental principles of fluid dynamics and extensive engineering practice.

To further investigate and validate the impact of extension lengths on fluid flow, we conducted a thorough literature review and referenced previous research findings. After comprehensive consideration of flow development, stability, and the need for analyzing internal flow patterns within the inlet section, we ultimately determined that the lengths of the inlet and outlet extensions should be set at four times the diameter of the pipeline. This choice aims to ensure that the fluid can fully develop and reach a stable flow state as it enters and exits the pipeline, while minimizing unnecessary energy losses and flow instabilities.

Additionally, the volute casing employs a daul volute structure, featuring two tongue baffles that may introduce hydraulic losses at the outlet of the impeller. This symmetric
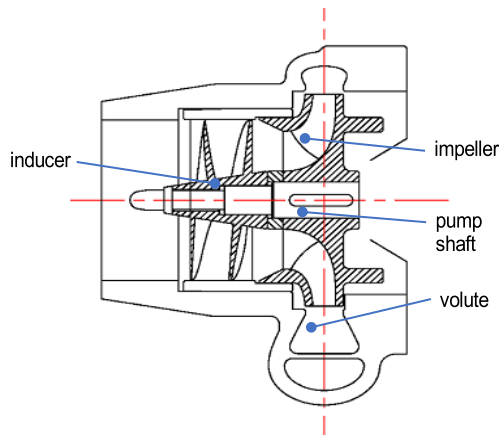
Fig. 4 Two-dimensional schematic diagram of the high-speed centrifugal pump
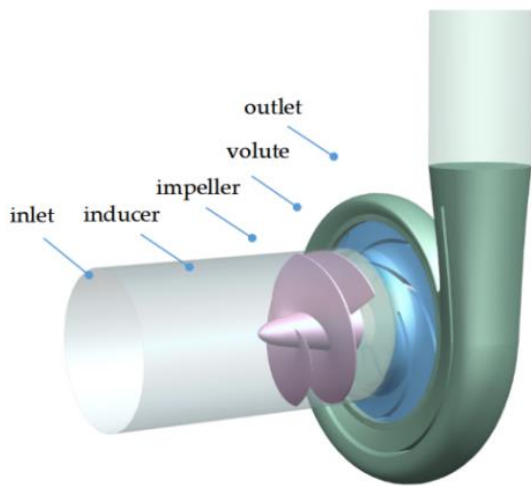

Fig. 6 Mesh generation of flow passage components

Fig. 5 Three-dimensional model diagram of high-speed centrifugal pump

Fig. 7 The grid of main flow components

arrangement creates a symmetrical pressure field around the impeller, thereby effectively reducing radial forces exerted on the centrifugal pump. The two-dimensional schematic diagram of the high-speed centrifugal pump is illustrated in Fig. 4, while the 3D computational model is presented in Fig. 5.

2.3.2 Grid Division

In numerical simulations, grid partitioning is crucial. Ensuring high-quality grids is fundamental for numerical calculations as they guarantee both computational efficiency and accuracy. In this study, the ICEM software is utilized for partitioning the computational domain for the entire flow field. Structured grid partitioning is utilized for the inlet section, inducer blade tip clearance, transition section, impeller, cavity, volute, and outlet section. Nevertheless, due to the intricate structure of the inducer, an adaptive unstructured grid is employed. Additionally, to ensure the accuracy of the numerical calculations, after setting the global grid, the local grid of the inducer is refined, such as refining the grid around the inlet and outlet corners. Figure 7 illustrates the overarching grid
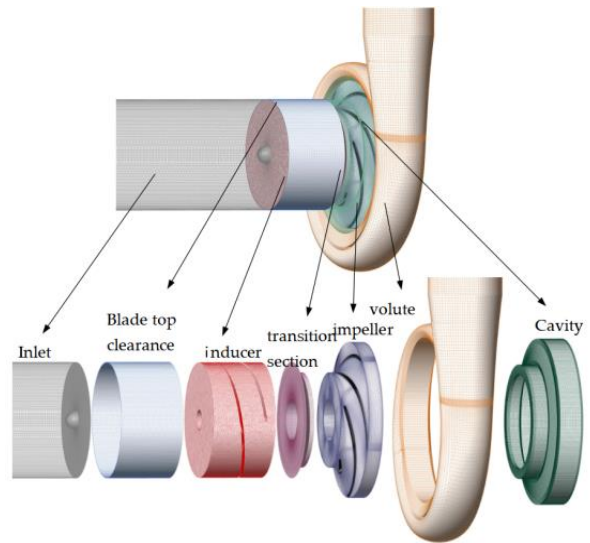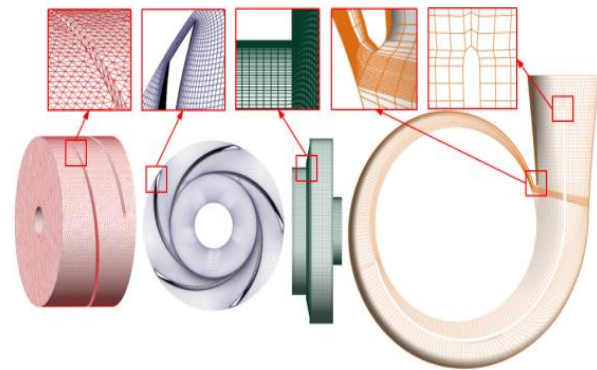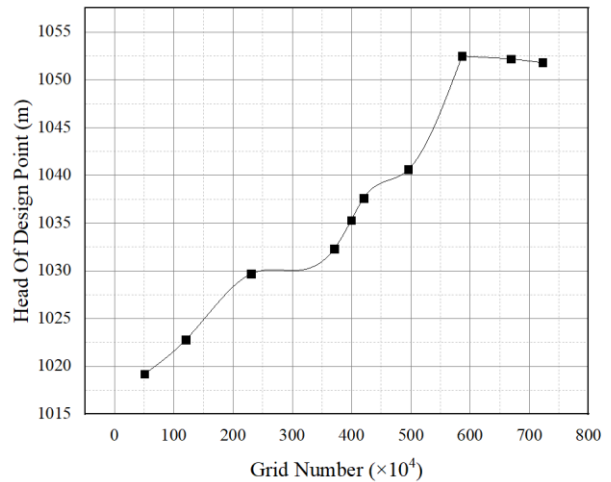

Fig. 8 Mesh Quantity & Head Curve

configuration of the model pump, while the grids of the main flow passing parts and their local enlargements are shown in Fig. 8.

Table 3 The grid independence test of pump

Grid Solutions	1	2	3	4	5
Number of grids	3994510	4957834	5863803	6687560	7225105
Head /m	1035.3	1040.6	1052.5	1052.2	1051.8

Table 4 The mesh number of overflowed components

Fow-passing parts	Number of grids
Inlet Section	804580
Blade Top Clearance	205685
Inducer	1101392
Transition Section	268298
Impeller	1079069
Cover Clearance	821305
Volute	932492
Outlet Section	650982

To improve the simulation accuracy and efficiency of boundary layer, this study conducted a grid assessment for the pump model. As presented in Table 3 and Fig 8, results from the table indicate that as the number of grids increases, the fluctuation of the head gradually diminishes, approaching a state of stability, the variation in the pump head at the rated condition is less than 0.5 % when the number of grids is more than 58.6 million. Finally, Scheme 3 is determined to be the optimal choice for subsequent calculations, The final mesh adopted is approximately 58.6 million to ensure accurate calculations.

2.3.3 Boundary Conditions

This study uses the ANSYS CFX to numerically analyze the centrifugal pump model described earlier, Initially, the grids for each component are imported into CFX-Pre for preprocessing. Next, the fluid domain is defined, with the impeller and inducer designated as rotating domains, while the remaining components are considered stationary. The basic conditions are as follows:"

(1) Calculation Medium: The external characteristic numerical calculation fluid medium is specified as water.

(2) Calculation Model: We adopted the SST k-ω model as turbulence model.

(3) Inlet Boundary Conditions: The total pressure inlet is used, and according to the design requirements, the total pressure at the pump's inlet is 0.4 MPa.

(4) Outlet Boundary Conditions: The corresponding mass flow rate was selected based on the design flow rate of the selected pump for the outlet conditions.

(5) Wall and Interface Conditions: We selected no-slip wall as boundary condition, and in steady-state calculations, the dynamic and stationary interfaces are set as a Frozen Rotor.

(6) Other Condition Settings: The number of iterations is set to 3000 steps. We have designated the Residual Type as RMS, ensuring that the residuals of the computational simulations are represented in a standardized and quantifiable manner, facilitating the analysis and interpretation of the simulation results. The advection scheme was configured to employ a second-order upwind method, while the turbulence numerics were set to high resolution. This configuration ensures accurate representation of fluid dynamics and turbulence characteristics, crucial for precise simulations and analysis in computational fluid dynamics (CFD) studies. the convergence is determined when the residual value is less than 10-5.

3. ANALYSIS OF RESULTS

3. 1 External Characteristic Curves of High-Speed Centrifugal Pumps Under Different Operating Conditions

Figure 9 illustrates the external characteristics curve of a high-speed centrifugal pump under different operating conditions. As the flow rate increases, the head curve exhibits a gradual decline, while the efficiency curve initially increases and then decreases. At the design condition of $1.0Q_d$, the pump reaches its optimum efficiency point. At this point, the head of the high-speed centrifugal pump reaches 1052.40 m, with an efficiency of 83.46%. The performance fully meets the design requirements and surpass the specified value by 8.81%. However, beyond this optimum efficiency point, especially under conditions of high flow rates, both the head and efficiency of the high-speed centrifugal pump experience a rapid decline.
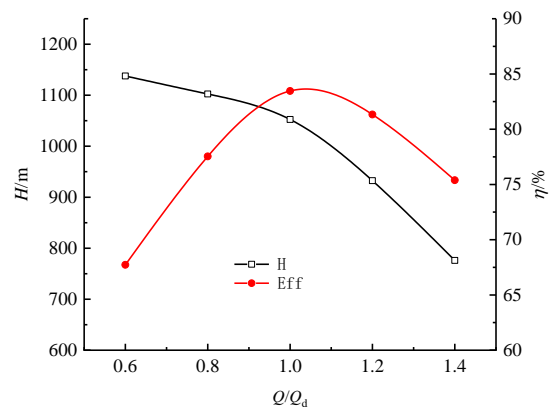

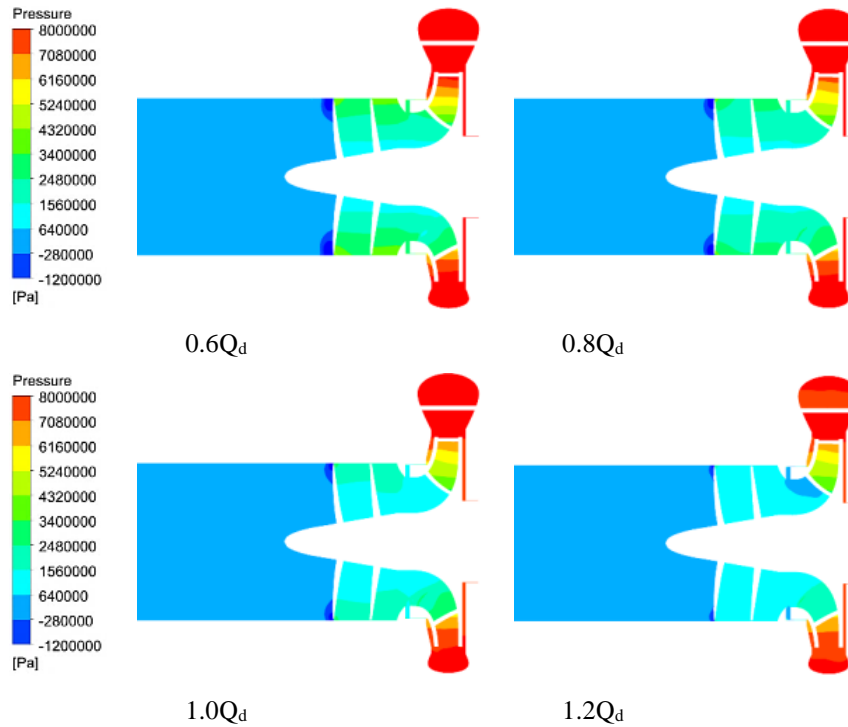**Fig. 9 The external characteristic curves of the high-speed centrifugal pump**

Fig. 10 The axial cross section pressure distribution of the high-speed centrifugal pump under different working conditions

3.2 Pressure Distribution of the High-Speed Centrifugal Pump Under Different Working Conditions

Figure 3. 2 depict the axial section pressure distribution of a high-speed centrifugal pump across various operating conditions. Under low flow rates of $0.6Q_d$, a significant low-pressure area is observed in leading edge of the impeller blades, making this region susceptible to cavitation. Within the impeller inducer channel, a pressure gradient exists, with higher pressure on the wheel side compared to the hub side. This gradient is primarily attributed to the increased load on the outer edges of the inducer blades during operation. Additionally, as flow rates increase, the internal pressure of the inducer wheel decreases gradually and uniformly." Since it's a 5-blade impeller, the pressure distribution on the axial section of the impeller is asymmetric, with a significant pressure gradient. The pressure at the impeller outlet is higher than at the inlet, and the inlet is prone to cavitation. The inlet pressure at the impeller diminishes progressively as the flow rate increases, attributable to the inducer wheel's influence. As the flow rate increases, the pressure difference between inner and outer sides of the double volute partition gradually become more apparent, with higher pressure on the inner side of the partition compared to the outer side. Although the double volute partition is designed to balance the pressure, its inherent asymmetry leads to higher pressure on the inner side. As, the impeller rotates at a high speed while the volute remains stationary, this asymmetry causes uneven pressure distribution within the volute. As flow rate increases, the pressure at the

impeller cover plate clearance gradually decreases due to the increased flow rate, this is mainly resulting in lower overall pressure within the pump. Consequently, the pressure difference across the pump wear ring clearance also decreases, reducing reversed flow within the pump clearance.

3.3 Velocity and Flow Distribution in High-Speed Centrifugal Pumps Under Different Working Conditions

To further investigate the flow characteristics within the entire flow path of a high-speed centrifugal pump, streamline plots and velocity distribution at selected sections of both inlet and outlet are generated for low-flow condition of $0.6Q_d$, the design point of $1.0Q_d$, and the high-flow condition of $1.2Q_d$, as depicted in Fig. 11, graphs reveal significant unstable flow and disturbances in the inducer wheel inlet passage at the low-flow condition of $0.6Q_d$. This is primarily due to the flow rate being below the design flow rate, resulting in an inlet liquid flow angle that is smaller than the inducer wheel blade inlet angle. Consequently, the fluid's absolute velocity exhibits a pre-swirl component aligned with the circumferential velocity, leading to flow separation on the blade's working surface. Under the influence of centrifugal force, the separated fluid recirculates back to the inducer wheel inlet, interfering with the main flow pattern. Additionally, a low-speed streamline is observed near the pipe wall at the volute outlet, indicating a tendency for vortex formation.

From the observed velocity profiles, it is evident that the fluid velocity at section A in the inlet section is notably lower
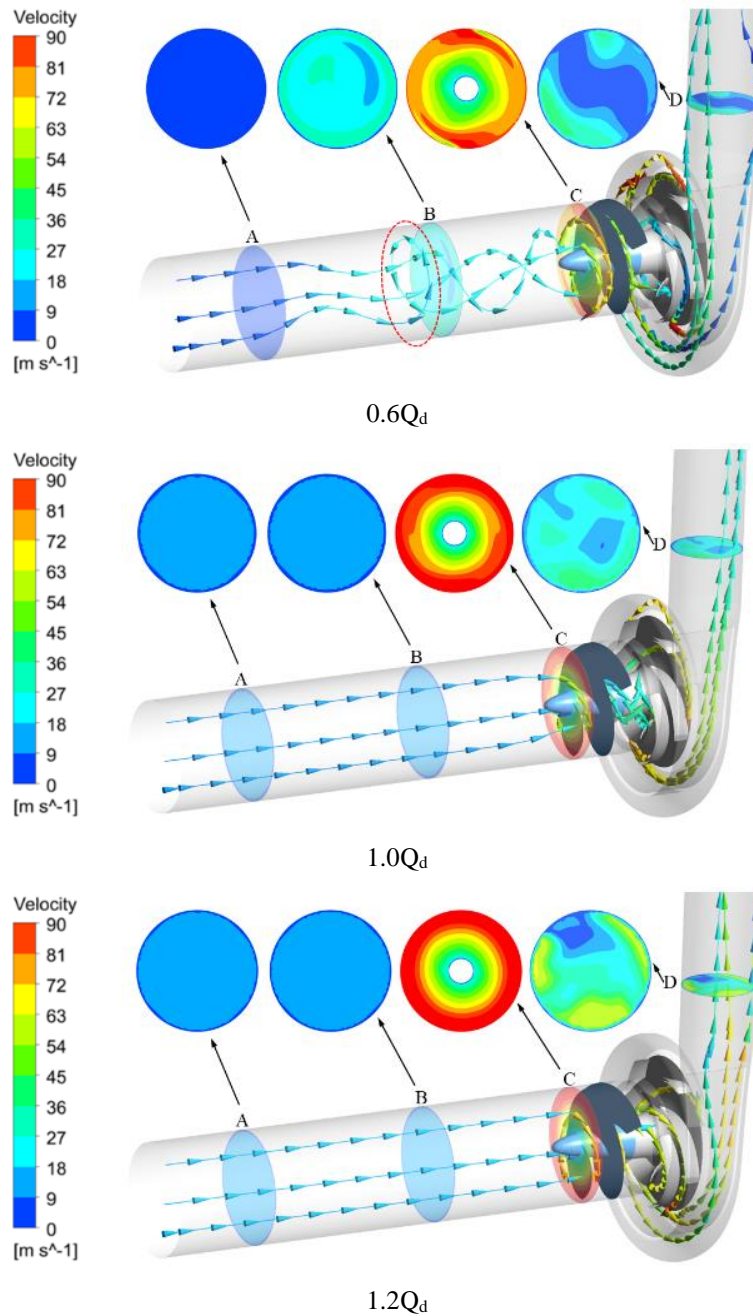
0.6Q_d

1.0Q_d

1.2Q_d

Fig. 11 The internal streamline and velocity section diagrams of the high-speed centrifugal pump under different working conditions

under the low-flow condition of 0.6Q_d. This is primarily attributed to the fact that section A is perpendicular to the streamlines, making it less susceptible to flow disturbances. Consequently, it primarily reflects the inlet velocity. However, as the flow rate increases to 1.0Q_d and 1.2Q_d, a significant rise in flow velocity is observed within the flow path. Interestingly, the velocity near the pipe wall remains relatively low under these higher flow rates.

This is mainly due to the large shear stress near the wall, resulting in increased resistance and decreased velocity.

Section B in the inlet section exhibits a local low-speed region and an asymmetric distribution due to the influence of the pre-swirl disturbances at the low-flow condition of 0.6Q_d. The velocity distribution becomes more uniform as the flow rate increases. Section C is located before the inducer wheel blade inlet, and the fluid velocity is significantly increased with a gradient distribution. The velocity increases layer by layer from the hub to the shroud. When flow rate increases, the high-speed area increases and becomes more uniformly distributed. Section D shows the velocity distribution of the
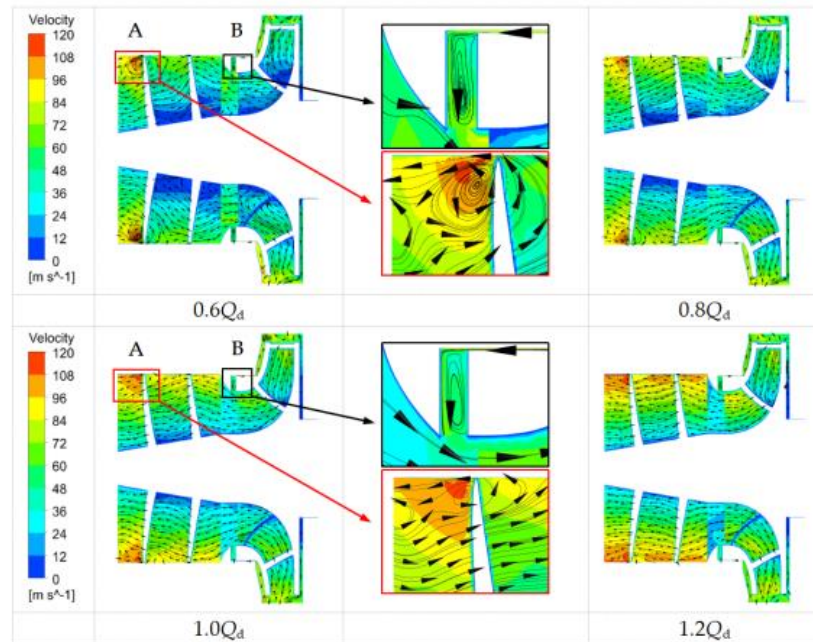
Fig. 12 The axial cross section velocity and streamline distribution of the high-speed centrifugal pump

outlet section. The overall velocity distribution exhibits an increasing trend with higher flow rates, resulting in a reduction of the low-speed region. However, the distribution exhibits irregularity, potentially linked to the flow division induced by the double volute partition.

Figure 12 illustrates the distribution of axial velocity and streamline within a high-speed centrifugal pump, depicting various operating conditions that encompass the inducer, impeller, and the gaps present in the front and rear chamber gaps. The streamline patterns clearly indicate the presence of reversed flow at the inducer's inlet wheel shroud. To facilitate a deeper comprehension of the reversed flow phenomenon, regions exhibiting significant reversed flow have been magnified. Specifically, the magnified view at point A indicates that a flow recirculation vortex occurs from the pressure side to the suction side of the inducer blade in the vicinity of the blade tip gap. This phenomenon arises from the inherent flow characteristics of the inducer itself. By deducing the impact loss formula at the wheel shroud inlet based on the Bernoulli equation, it can be inferred that reversed flow will occur when there is a relatively small head loss. Combining this observation with Fig. 10, it can be concluded that there is a low-pressure region at the impeller inlet wheel rim due to the presence of reversed flow. Turning to the magnified view at point B, it can be observed that significant reversed flow occurs at the gap between the impeller front shroud and the cover plate, generating a recirculation vortex. This is attributed to the pressure disparity between the impeller outlet (high pressure) and the inlet (low pressure), causing the fluid to flow from the high-pressure region to the low-pressure region. The reversed flow phenomena at the inducer inlet

wheel shroud and the front shroud gap diminish gradually as the flow rate increases.

From the velocity distribution, it is evident that at lower flow rates ($0.6Q_d$ and $0.8Q_d$), the speed is higher at the inducer's inlet wheel rim and lower at the hub region. The fluid velocity is not uniform, and the velocity inside the impeller is also lower. As the flow rate gradually increases, the velocity distribution in the flow path becomes more uniform, and significant velocity gradients occur. The wheel shroud of the inducer transforms into the high-speed region, while the area proximate to the hub transforms into the low-speed zone.

3.3 Vorticity Distribution of High-Speed Centrifugal Pumps Under Different Operating Conditions.

Using the Q-criterion, a common method for vortex identification, we can accurately determine the vortex structures within a fluid. As seen in the vorticity distribution diagram, regions of high Q-values typically represent vortex cores or intense vortex structures. It can be seen from Fig. 13, in the axial cross-section of the high-speed centrifugal pump under different operating conditions, the vorticity distribution is evident. Initially, under low flow conditions, there is a prominent concentration of vorticity at the leading edge of the inducer's blade tip. This is due to the increased instability of fluid flow caused by the low-pressure region, resulting in stronger vortices. These vortices are represented in the diagram by high q-value regions, indicating deeper colors.

As the flow rate increases, the concentrated vorticity region at the leading edge of the inducer blade tip gradually shrinks and shifts towards the blade tip gap. This
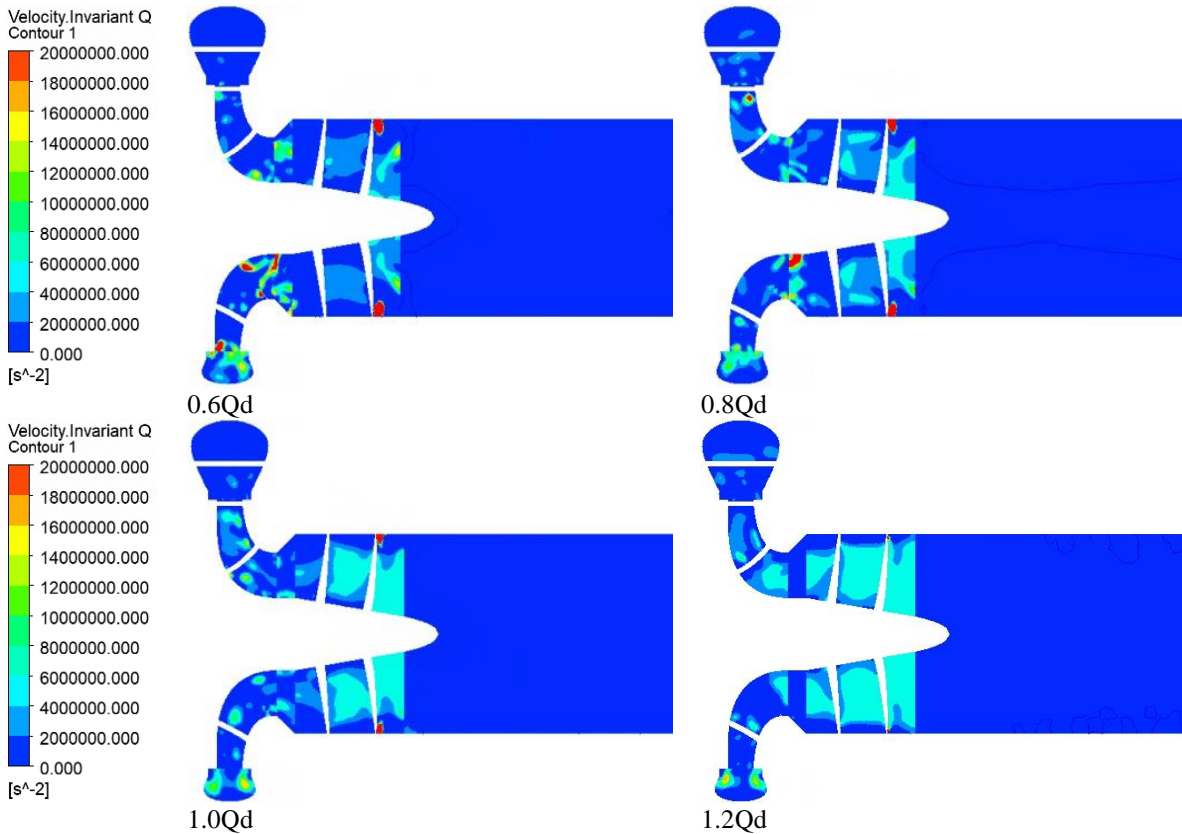
Fig. 13 Distribution of axial section vorticity in high-speed centrifugal pumps under different operating conditions

suggests that as the flow rate increases, the fluid flow becomes more uniform, reducing the intensity and extent of vortices. Within the inducer's flow channel, the distribution of vorticity also undergoes changes as the flow rate increases. At low flows, the vorticity distribution within the channel is relatively uneven, with distinct vortex structures. However, as the flow rate increases, the vorticity distribution within the channel gradually becomes more uniform, with the vortex structures weakening.

Regarding the impeller section, the vorticity at the inlet and outlet also varies with increasing flow rate. At low flows, these regions exhibit strong vorticity, indicating significant flow instability. As the flow rate increases, the vorticity in these regions gradually weakens, leading to more stable flow. Furthermore, the vorticity distribution on both sides of the double-volute divider plate is also influenced by the flow rate. At low flows, there is a significant difference in vorticity between the inner and outer sides of the divider plate. However, as the flow rate increases, this difference gradually diminishes, resulting in a more uniform vorticity distribution.

Lastly, it is noteworthy that the vorticity at the gap between the impeller's front cover and the plate also decreases as the flow rate increases. This could be attributed to the more uniform pressure distribution within

the pump as the flow rate increases, leading to a reduction in vortex strength in this region.

4. IMPACT OF INDUCED WHEEL WRAP ANGLE ON CENTRIFUGAL PUMP PERFORMANCE

4.1 Model Solution

The main purpose of the inducer wheel is to improve the cavitation performance of the pump. In this section, the impeller head is increased by changing the blade wrap angle of the inducer wheel. Three sets of blade wrap angles, 230°, 240°, and 250°, were designed for the inducer wheel while keeping other parameters constant, as shown in Fig. 14. Numerical calculations were conducted for these three sets of designs.

4.2 External Characteristic Curves OF Centrifugal Pumps with Induced Wheel Vane Wrap Angle Under Different Operating Conditions

The head efficiency (ηh), serving as a crucial performance parameter for pumps, reflects the effective degree of energy conversion during fluid transportation. According to the fundamental theory of pumps, the head efficiency can be expressed as a function of flow variables such as flow rate (Q), head (H), and rotational speed
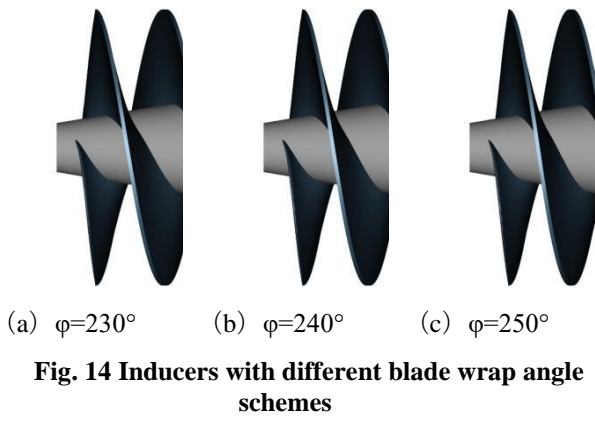
(a) φ=230° (b) φ=240° (c) φ=250°

Fig. 14 Inducers with different blade wrap angle schemes

Fig. 15 Hydraulic performance curves of centrifugal pumps with different inducer blade wrap angles

(N).The specific expression is as follows:

$$\eta_h = \frac{\rho g Q H}{P_{in}}$$

The following parameters are defined as follows: η_h represents the head efficiency; ρ denotes the density of the fluid; g stands for the gravitational acceleration; Q represents the flow rate, indicating the volume of fluid pumped per unit time; H signifies the head, which represents the increase in pressure energy head of the fluid after being pumped; and Pin is the input power of the pump.

Power (P) typically has two common expressions, one based on mechanical principles and the other based on electrical principles. In the context of pumps, our focus is primarily on mechanical power, which can be expressed as:

$$P = \frac{QH\rho g}{3600 * 1000}$$

This expression is utilized to calculate the power required or generated by a pump during its operation. The magnitude of power is determined by the fluid's velocity, pressure head, and physical properties. In this context, P represents the power, indicating the work performed by the pump per unit time; Q denotes the flow rate; H represents the head; ρ is the density of the fluid; g is the gravitational acceleration.

Figure 16 depicts Head & efficiency changes with flow rate for different induced impeller blade wrap angles in a centrifugal pump. Regarding the head curve, the trends of head variation among different configurations are largely consistent. Exhibiting high lift characteristics at low flow rates, but as the flow rate gradually increases, the head significantly decreases, exhibiting a negative correlation between head and flow rate. At $0.6Q_d$ and $1.0Q_d$, the head values for the different configurations are nearly equal. At $0.8Q_d$, the blade wrap angle φ=250° corresponds to the highest head, while at $1.2Q_d$, the blade wrap angle φ=230° corresponds to the highest head, with a maximum difference of 20.98 m.

Regarding the efficiency curve, the variations are similar

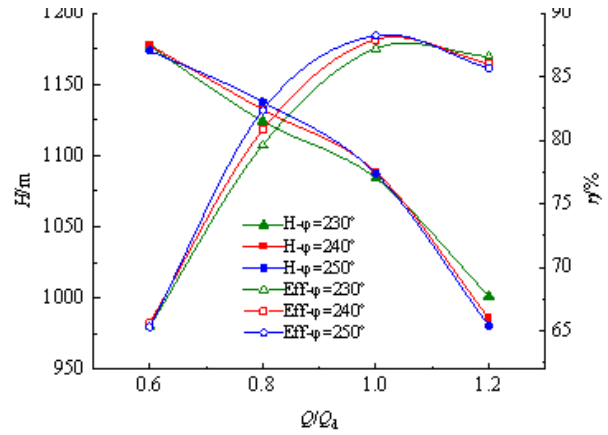among different configurations. They all follow an increasing-decreasing trend with increasing flow rate. The efficiency rapidly increases with flow rate and reaches its maximum at the design operating point. Subsequently, it gradually decreases. The highest efficiency points for all three configurations are located at $1.0Q_d$, with the most noticeable difference observed at $0.8Q_d$, with a maximum deviation of 2.74%. Within the range of $0.6Q_d$ to $1.0Q_d$, the blade wrap angle φ=250° exhibits relatively higher efficiency. However, after the design operating point of $1.0Q_d$, it decreases rapidly, while the efficiency curve corresponding to the blade wrap angle φ=240° remains relatively stable.

In summary, the inducer blade wrap angle has a significant impact on the hydraulic performance of centrifugal pumps. Regarding head, smaller blade wrap angles exhibit larger fluctuations compared to other configurations, which are not ideal for operation under varying working conditions. In terms of efficiency, it increases with an increase in wrap angle at low and design flow rates. However, at high flow rates, efficiency decreases with an increasing wrap angle. Therefore, selecting a moderate blade wrap angle is crucial for achieving optimal overall performance of the centrifugal pump.

Based on numerical calculations, the operational parameters of the inducer wheel under different blade wrap angles and working conditions are obtained to draw external characteristic curves with varying performances, as shown in Fig. 16.

From Fig. 16 (a), it can be observed that the head variation trend of the inducer wheel remains consistent across different scenarios. At flow rate less than $0.8Q_d$, the head increases with an increase in flow rate. When the flow rate exceeds $0.8Q_d$, head curve exhibits a sharp decline, and this decrease becomes more noticeable as the blade wrap angle of the inducer wheel increases. This phenomenon can be attributed to the fact that with larger wrap angles, the relative fluid flow angle decreases, resulting in a decline in heads.
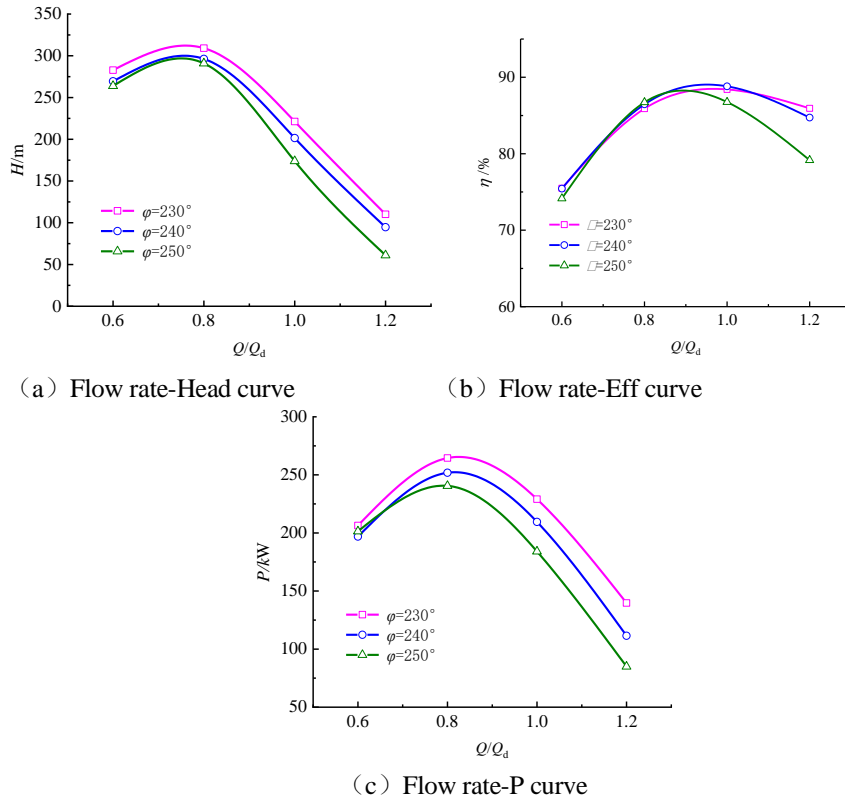
（a）Flow rate-Head curve

（b）Flow rate-Eff curve

（c）Flow rate-P curve

Fig. 16 Hydraulic performance curves of inducer with different inducer blade wrap angles

From Fig. 16 (b), it is evident that the efficiency curves of the inducer wheel for different wrap angles exhibit a similar pattern as the flow rate varies. Initially, efficiency increases rapidly with increasing flow rate, peaking near the design operating point. Subsequently, it varies slowly. However, at higher flow rates, the efficiency decreases significantly, with larger wrap angles exhibiting a greater decline. At the design flow rate of $1.0Q_d$, the configuration with a wrap angle of $\varphi=240°$ achieves the highest efficiency, surpassing the efficiency of the $\varphi=250°$ configuration by 2.07%. At the high flow condition of $1.2Q_d$, the $\varphi=250°$ configuration exhibits a notable drop, reaching a maximum difference of 8.56% compared to the peak efficiency. This decrease in efficiency is attributed to the enlarged wrap angle, resulting in a narrower flow passage which intensifies the constraining effect on the fluid by the inducer wheel. Additionally, friction losses on the blade surface further contribute to the reduced efficiency.

From Fig. 16 (c), it can be observed that the power variation trend of the inducer wheel for different blade wrap angles is generally consistent with the flow rate. Prior to $0.8Q_d$, the power increases with increasing flow rate, reaching its peak at $0.8Q_d$, and then gradually decreases as the flow rate continues to rise. It can be seen that power curves vary significantly among different configurations, indicating that the blade wrap angle plays a substantial role in influencing the inducer wheel power. Larger wrap angles result in lower power, while smaller wrap angles

lead to higher power. This is because an increased wrap angle results in longer blades, thereby increasing the frictional resistance experienced by the fluid and consequently causing a power decline.

In summary, a smaller blade wrap angle enhances the head and efficiency of the inducer wheel. However, extremely small wrap angles can compromise the constraint on the fluid within the flow passage. Conversely, larger wrap angles lead to a rapid decline in the head of the inducer wheel with increasing flow rate, potentially resulting in negative head and inability to meet varying operational demands. Consequently, an optimal blade wrap angle exists that maximizes the hydraulic performance of the inducer wheel. In this study, an inducer model with a blade wrap angle of 240° was chosen, exhibiting superior hydraulic performance.

Upon further analysis of the relationship between the blade wrap angle of the inducer wheel and its efficiency and head, we observe an intriguing trend. Under rated flow conditions, initially increasing the blade wrap angle within a certain range enhances the flow dynamics within the inducer, minimizing adverse flow phenomena such as flow separation and vortices. This improved flow pattern leads to higher inducer efficiency. This is because a larger blade wrap angle better constrains and guides the fluid, enabling it to flow closer to the blade profile, thus reducing hydraulic losses.
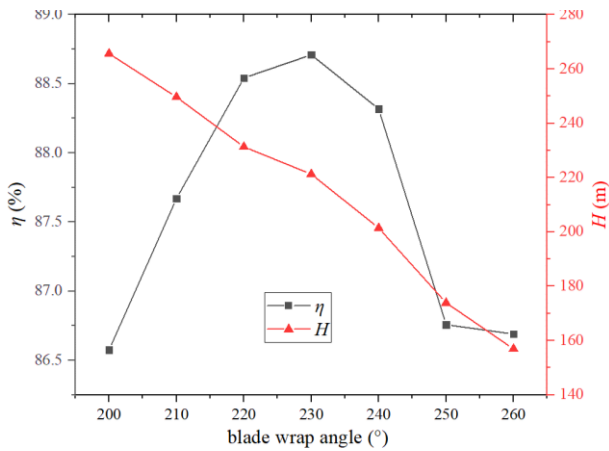
However, beyond 230°, efficiency begins to decline.

Fig. 17 Blade Wrap Angle vs. Head and Efficiency Dual-Y-Axis Correlation Chart

One plausible explanation is that as the blade wrap angle continues to increase, the friction losses within the impeller passage increase. The longer flow path and larger contact area between the fluid and the blades contribute to increased frictional losses. Additionally, an overly large blade wrap angle may complicate the fluid flow within the passage, increasing flow resistance and further reducing efficiency.

On the other hand, the head monotonically decreases with the increase in blade wrap angle under rated flow

conditions. This is due to changes in fluid dynamic characteristics, worsened inlet flow conditions, and reduced energy conversion efficiency. This observation underscores the complexity of the relationship between blade wrap angle and pump performance, highlighting the need for careful optimization to achieve desired efficiency and head characteristics.

4. 3 Effect of Blade Wrap Angle on Internal Flow in Induced Wheel under Different Operating Conditions

Numerical simulations were conducted for three distinct blade wrap angles of the inducer pump models, across various working conditions, to derive the blade static pressure distribution contour maps depicted in Fig. 18, Fig. 19, and Fig. 20. Given the similarity in pressure distribution among the blades, only one blade is selected for the static pressure analysis.

Figure 18 depicts the static pressure distribution contour map for an inducer blade with a wrap angle of 230°, Figure 4.5 illustrates the same for a blade with a wrap angle of 240°, and Figure 20 presents the contour map for a inducer blade with a wrap angle of 250°.

As Fig. 18 through Fig. 20 demonstrate, it is evident that the blade length increases with a larger wrap angle, while maintaining a constant axial length of the induced wheel. Furthermore, the static pressure distribution among the blades with different wrap angles exhibits a consistent trend as the flow rate increases. From the inlet to the outlet
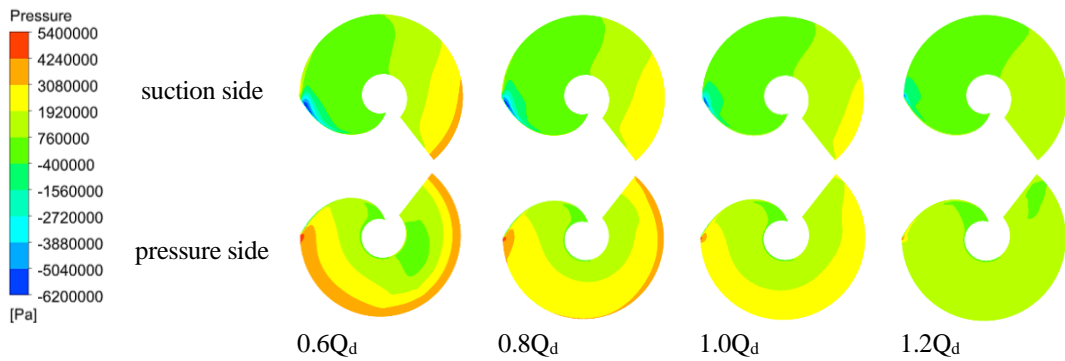

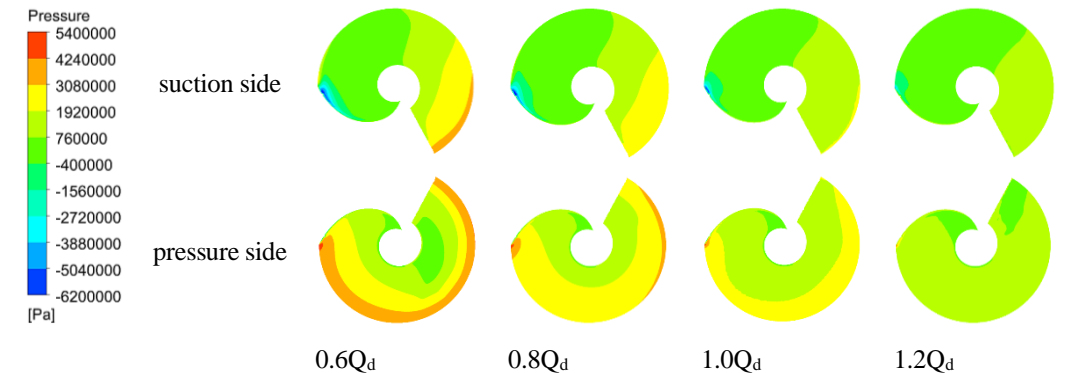**Fig. 18 The static pressure distribution of inducer blade under different conditions at φ=230°**

Fig. 19 The static pressure distribution of inducer blade under different conditions at φ=240°

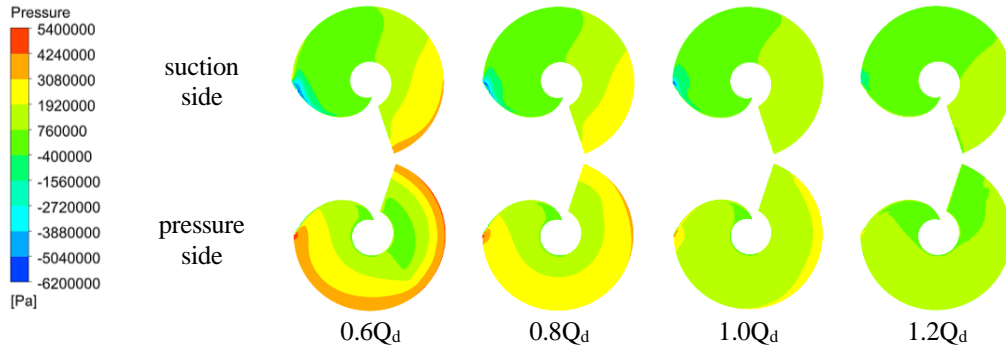**Fig. 20 The static pressure distribution of inducer blade under different conditions at φ=250°**

of the inducer wheel, there is a gradual increase in the static pressure on the suction side of the blade. Specifically, at the inlet edge of induced wheel, a localized low-pressure area emerges primarily on the outer edge, rendering this region particularly susceptible to cavitation. Conversely, at outer edge near blade outlet, the pressure is elevated. As the flow rate increases, both the low- and high-pressure zones gradually diminish, leading to a more uniform static pressure distribution. On the pressure side of the blade, the static pressure gradually rises in a gradient manner, moving towards the shroud from the hub. Notably, the high-pressure zone is concentrated on the outer edge of the blade, and this gradient is particularly pronounced under low flow conditions. With the increase in flow rate, the high-pressure zone gradually shrinks towards outer edge, the pressure gradient decreases, resulting in a more uniform static pressure distribution in all regions. Additionally, the static pressure on the pressure side of the blade is always higher than the static pressure on the suction side. At the blade inlet edge, the pressure side exhibits a high-pressure zone, while suction side shows a low-pressure zone. This can lead to flow reversal at the blade tip due to pressure differences, which is unfavorable for the stable operation of the inducer wheel.

By comparing the static pressure distributions of the inducer blade across various wrap angles under identical working conditions, it can be concluded that as the wrap angle increases, both the low- and high-pressure zones on the suction side undergo a reduction, resulting in gradually decreasing pressure gradients. The most uniform pressure distribution is observed at a wrap angle of 250. Notably, at low flow conditions, the static pressure variation on the suction side is relatively minor, whereas significant alterations in the static pressure distribution become evident at the design point flow rate and high flow conditions. The static pressure on the pressure side decreases gradually with an increase in wrap angle, and both the high-pressure zone and the low-pressure zone expand from the hub to the shroud

To further delve into the impact of blade wrap angle on the performance of the inducer wheel, an analysis is conducted on the static pressure distribution across various sections of the wheel passage. Figure 21 illustrates the static pressure distribution at section A, B, and section C
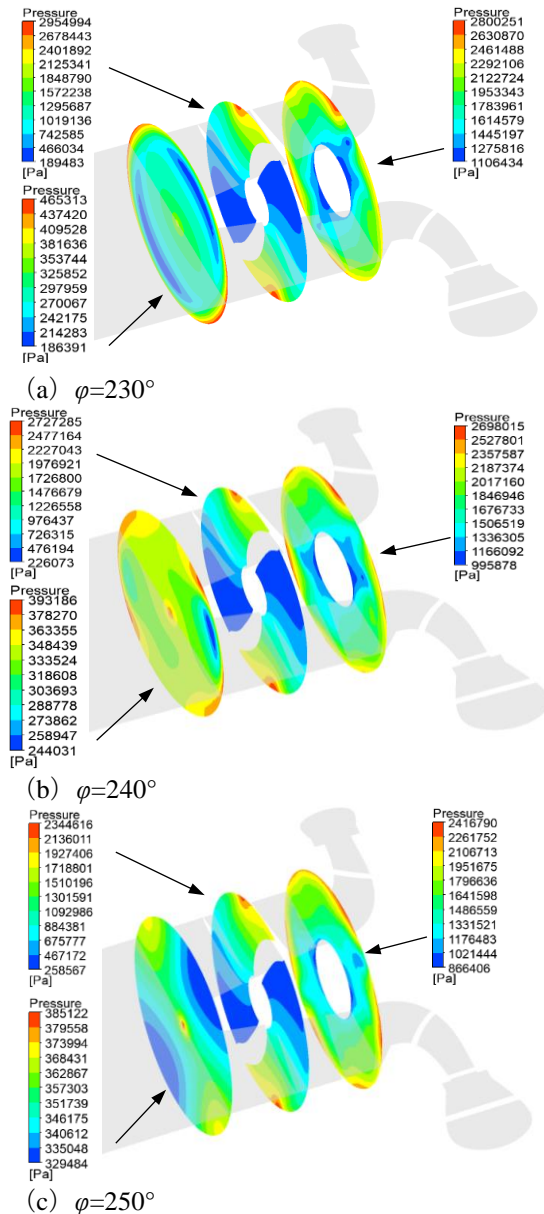
of the inducer wheel passage.

（a） φ=230°

（b） φ=240°

（c） φ=250°

Fig. 21 Effect of induced wheel blade wrap angle on internal impeller flow under different operating conditions

Observing Fig. 21, it becomes evident that the static pressure distribution at the inlet section A of the inducer wheel undergoes significantly variations as the wrap angle increases. Firstly, the position of the low-pressure zone varies depending on the wrap angle. At small wrap angle (e.g., φ=230°) and larger wrap angles (e.g., φ=250°), the low-pressure zone is symmetrically distributed near the outer wall of the passage, with a more prominent size. This asymmetry is primarily attributed to a flow reversal at the blade inlet edge. Concurrently, the high-pressure zone is symmetrically disposed on both sides of the passage, perpendicular to the low-pressure zone, with a partial high-pressure zone at the head of the diffuser cone. However, at a wrap angle of φ=240°, the low-pressure zone at the corresponding inlet section A is reduced in size, while the high-pressure zone exhibits a more uniform distribution along the outer edge of the passage. This configuration results in a reduced flow reversal at the inlet of the inducer wheel, enabling a smoother fluid entry. Secondly, by referring the pressure scale, it is noticeable that the minimum static pressure at the inlet section for the small wrap angle case is 186391 Pa, with a maximum static pressure of 465,313 Pa. This significant pressure difference can potentially lead to flow instability. Nevertheless, as the wrap angle increases, the pressure difference gradually diminishes, leading to a more stable fluid flow at the inlet section of the inducer.

The static pressure distribution at section B shows no significant variation with the increase in wrap angle. A large pressure gradient is observed, with lower pressure on the suction side at the inlet and gradually increasing towards the outlet. The static pressure on the pressure side is always higher than the static pressure on the suction side, which is consistent with the static pressure distribution on a single blade. For the small wrap angle case, the maximum static pressure at the section is 2,954,994 Pa, and the minimum static pressure is 189,483 Pa, resulting in a pressure difference of 2,765,511 Pa. For the large wrap angle case, the maximum static pressure is 2,344,616 Pa, the minimum static pressure is 258,567 Pa, and the pressure difference is 2,086,049 Pa. The pressure difference on the section decreases as the wrap angle increases, and the static pressure distribution becomes more uniform.

At section C of the inducer wheel, the area of the low-pressure zone diminishes as the wrap angle expands, with the low-pressure region distributed uniformly at the hub of the inducer wheel outlet. Conversely, the high-pressure zone is concentrated near the passage wall, attributed to the centrifugal force exerted during the inducer wheel's operation. This centrifugal force causes the fluid to be ejected towards the wall, leading to a localized high-pressure condition. Notably, from the scale, it is evident that both the peak and nadir pressure values decrease with increasing wrap angle, although the pressure difference remains relatively stable.

The existence of a low-pressure zone on the blade is susceptible to inducing cavitation, and an enlarged low-pressure zone area further elevates the probability of cavitation occurrence. In summary, by comparing the static pressure distribution across the passages corresponding to three distinct blade wrap angles, it is found that the wrap angle of φ=240° exhibits the smallest low-pressure zone at the inlet, suggesting superior overall performance. Therefore, from the perspective of optimizing the inducer wheel itself, a blade wrap angle of 240° is deemed the optimal design choice.

The distribution of turbulent kinetic energy across the mid-section of the impeller is depicted in Fig. 22. comparing different blade wrap angle configurations., the figure reveals that the turbulent intensity at the impeller outlet surpasses that at the inlet, suggesting stronger turbulence at the outlet.

As flow velocity increases, the turbulent kinetic energy at the impeller's mid-section decreases across all three schemes. Notably, at lower flow rates ($0.6Q_d$ and $0.8Q_d$), the turbulent kinetic energy decreases with a larger wrap angle. However, at the design point ($1.0Q_d$) and higher flow rate ($1.2Q_d$), the turbulent kinetic energy exhibits an upward trend with an increase in wrap angle, particularly evident at the $1.2Q_d$ condition. This trend is more pronounced at the impeller inlet, indicating that the blade wrap angle size significantly impacts fluid flow at the inlet. Therefore, during the design phase, it is crucial to select an appropriate blade wrap angle to minimize its impact on the impeller performance.

To further investigate the impact of the blade wrap angle on the performance of centrifugal pump, we analyze the numerical results of the three schemes under varying operating conditions using streamline analysis, as demonstrated in Fig. 23.

From the figure, it can be observed that at the $0.6Q_d$condition, due to the low flow rate, the fluid flow becomes chaotic. Additionally, separation occurs within volute, resulting in significant vortices at the impeller inlet. As the blade wrap angle increases, the vortices become more pronounced, leading to a decrease in flow velocity and, subsequently, a reduction in impeller performance. The inclusion of diffusers in the double volute gives rise to separation vortices, which contribute to unstable flow conditions at the outlet.

As the flow rate increases, the streamlines within the impeller and volute become increasingly smoother. At the $0.8Q_d$ condition, indicating a more stable flow. However, some bending of the streamlines inside the impeller passage, and the vortices at the volute outlet decrease.

At the design point ($1.0Q_d$), the flow within the impeller becomes even more regularized, as evidenced by smoother streamlines. Nevertheless, for a wrap angle of 250°, irregularities in the streamlines persist within the impeller passage, and separation vortices are still observed at the outlet.
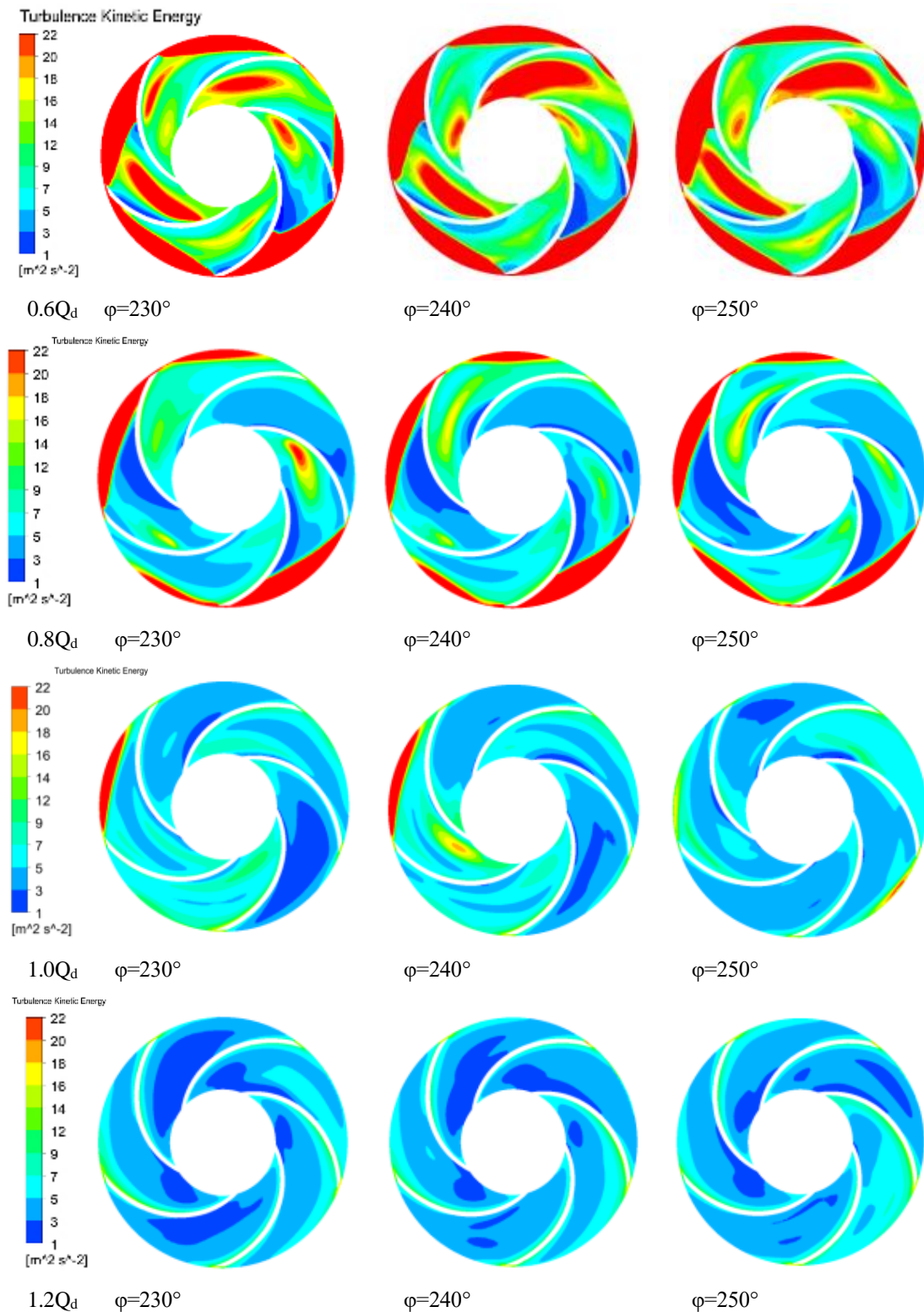
Fig. 22 The turbulent kinetic energy distribution of impeller section under different schemes

At $1.2Q_d$, the flow streamlines inside the impeller passage are completely smooth, and the flow velocity significantly increases. However, the separation vortices at the outlet of the volute become more prominent, especially with an increase in the wrap angle. This leads to a poor conditions and reduced flow stability within the centrifugal pump. Therefore, at a wrap angle of 250°, the internal flow stability of the centrifugal pump deteriorates, resulting in lower head and efficiency.

In conclusion, the blade wrap angle of the inducer has a certain influence on both the inducer itself and the performance of the centrifugal pump. A wrap angle of 240° corresponds to better performance of the inducer and the centrifugal pump. Therefore, in the following chapters, the analysis will be conducted using the scheme with a blade wrap angle of 240°.
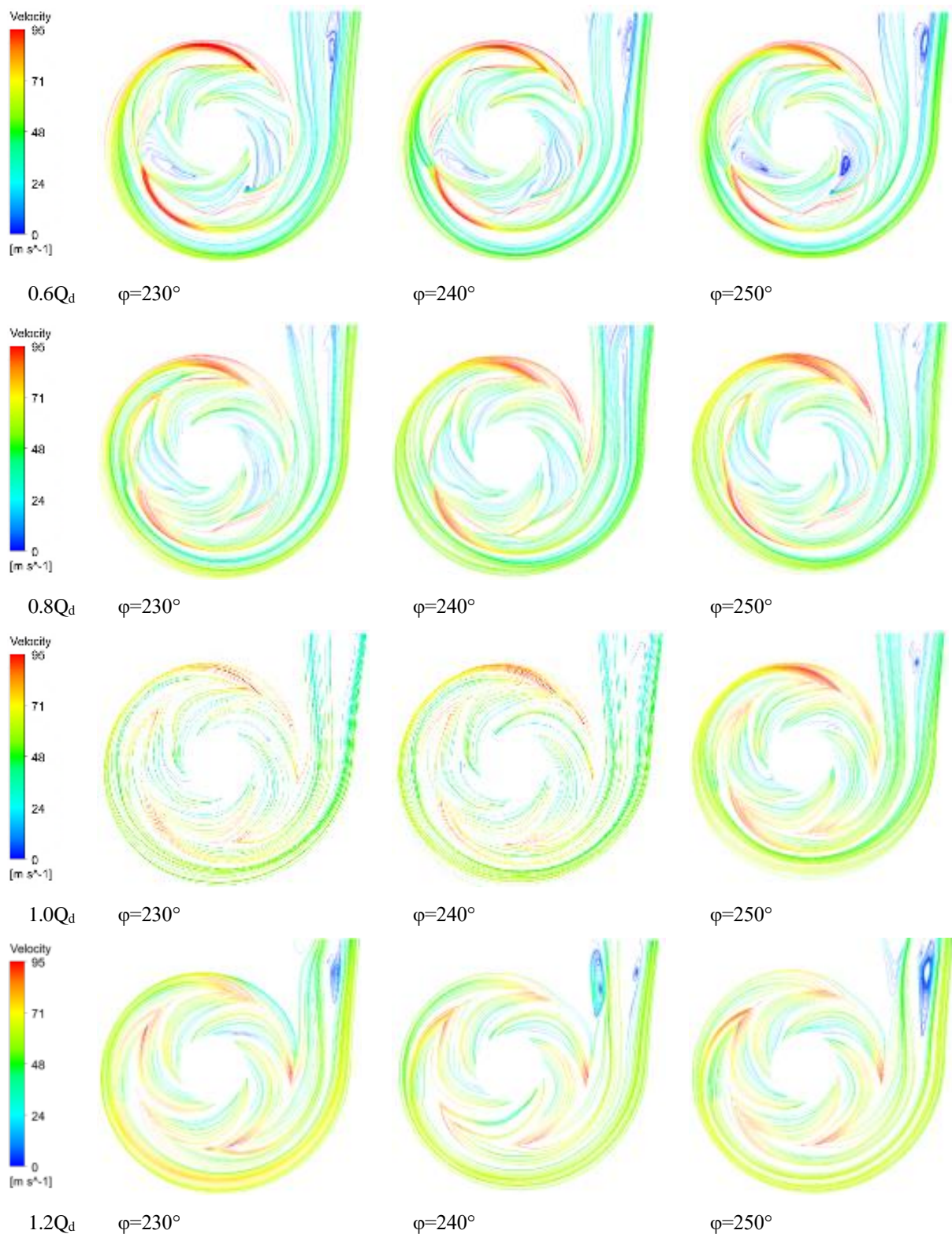
| 0.6Q$_d$ | φ=230° | φ=240° | φ=250° |

| 0.8Q$_d$ | φ=230° | φ=240° | φ=250° |

| 1.0Q$_d$ | φ=230° | φ=240° | φ=250° |

| 1.2Q$_d$ | φ=230° | φ=240° | φ=250° |

Fig. 23 The Streamline distribution of impeller volute section under different schemes

5. IMPELLER INLET SIZE ON THE CENTRIFUGAL PUMP PERFORMANCE EFFECTS

5. 1 Model Solution

The inducer wheel plays a crucial role in the cavitation performance of centrifugal pumps, as demonstrated in the previous section, where an optimized inducer wheel was achieved. Considering the dimensions of the connection between the inducer wheel and the impeller, as well as the goal of enhancing the hydraulic performance of the centrifugal pump, this section examines the impact of the varying the inlet diameter of the centrifugal pump impeller on its performance. With all other parameters held constant, three distinct impeller
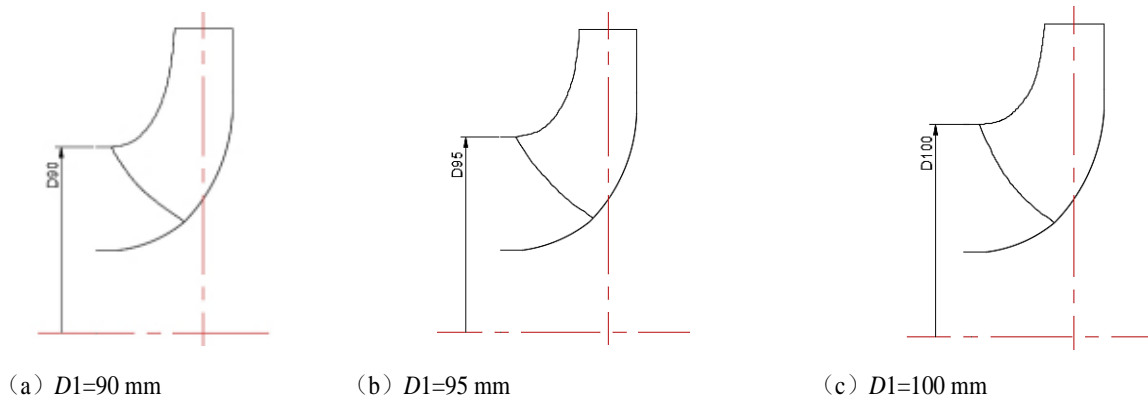
（a）*D*1=90 mm   （b）*D*1=95 mm   （c）*D*1=100 mm

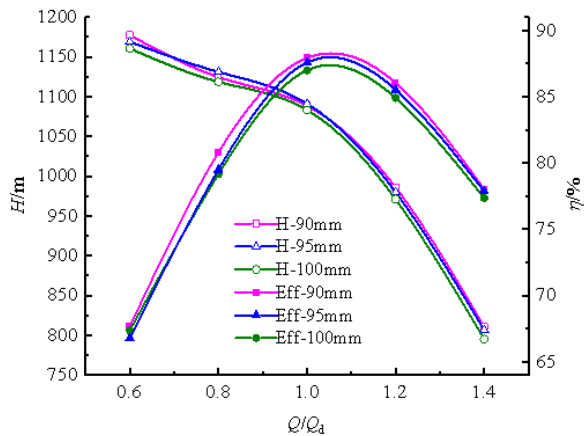**Fig. 24 The shaft surface diagrams of the impeller under three schemes**

Fig. 25 The external characteristic curves of high-speed centrifugal pumps with different impeller inlet diameters

configurations were created by varying the inlet diameter to 90 mm, 95 mm, and 100 mm, respectively. The axial projection diagrams for each of these impeller configurations are presented in Fig. 24.

5. 2 External Characteristics Analysis

the external characteristic curves of high-speed centrifugal pumps with varying impeller inlet diameters are depicted in Fig. 25. Upon examining the graph, it becomes evident that the pump head and efficiency follow similar trends across the different impeller inlet diameter configurations. As the flow rate gradually increases, the head experiences gradual decreases at first, but the rate of this decrease intensifies beyond the design operating point. Conversely, the efficiency experiences a rapid increase with increasing flow rate, peaking at the design operating point before gradually tapering off.

Upon comparing the head and efficiency curves of the centrifugal pump across various schemes, it is evident that the pump's head remains relatively similar for impeller inlet diameters of 90 mm and 95 mm. However, the impeller with an inlet diameter of 100 mm exhibits the lowest head. Regarding efficiency, the high-speed centrifugal pump experiences a decrease in efficiency with an increasing impeller inlet diameter. This decrease

is most pronounced near the design operating point. Overall, the impeller inlet diameter has a relatively minor impact on the pump's head but has a more significant effect on efficiency. Specifically, a smaller impeller inlet diameter leads to higher efficiency. In this context, the pump performs optimally with an impeller inlet diameter of 90 mm.

5.3 Analysis of Internal Flows

5.3.1 Impeller Pressure Distribution

Figure 26 displays the pressure distribution across impellers with different inlet diameters under different operating conditions. The graph reveals a consistent pattern in pressure distribution along different schemes, exhibiting a uniform distribution along the circumferential direction. The pressure gradually rises from the hub towards the blade tip, with the low-pressure area concentrated primary at the inlet of the impeller blades and the high-pressure area are situated at the outlet.

Although there is a degree of asymmetry in the distribution, it becomes more symmetric at the high flow rate operating point of $1.4Q_d$,

Upon comparing the pressure distribution among impellers of different schemes under identical condition, it becomes evident that at $0.6Q_d$ operating point, the impeller with a 90 mm diameter exhibits a larger low-pressure region at the blade inlet. As diameter increases, the relative size of the low-pressure region decreases. From the $0.8Q_d$ to $1.4Q_d$ operating points, an increase in in inlet diameter leads to an expansion of the low-pressure region at the impeller inlet., This suggests that pumps are less susceptible to cavitation when the low-pressure region is smaller, indicating that the impeller with a 90 mm inlet diameter exhibits the most superior cavitation performance.

When comparing the pressure distribution of the identical scheme across varying operating conditions, it is found that the static pressure fluctuation within the impeller remain consistent among all three schemes. As the flow rate increases, the area of the low-pressure region at the impeller inlet experiences an initial decrease, followed by a subsequent increase. Conversely, the area of the high-pressure region at the impeller outlet gradually decreases. The smallest low-pressure region is observed at the $0.8Q_d$ operating point; thereafter the low-pressure
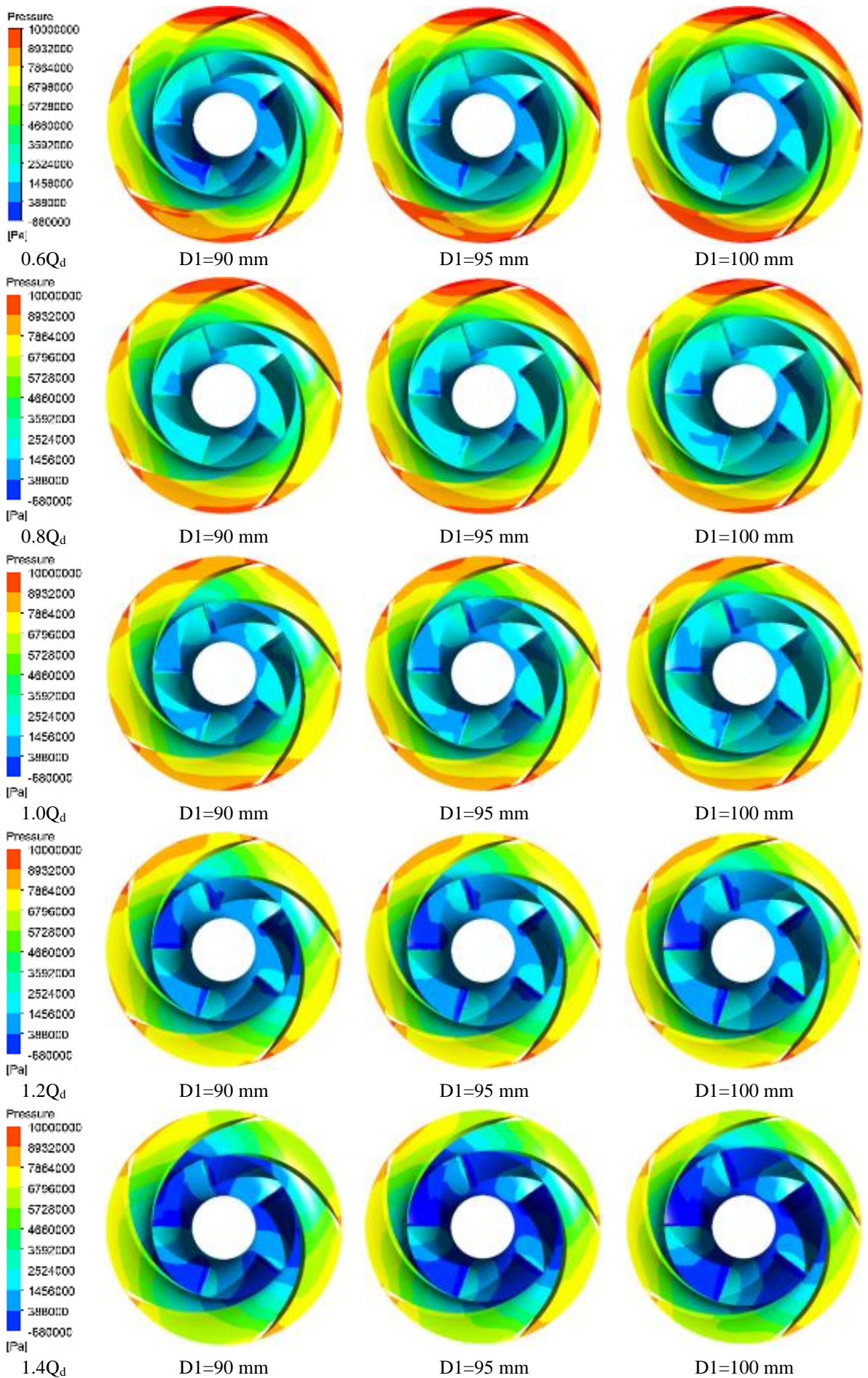
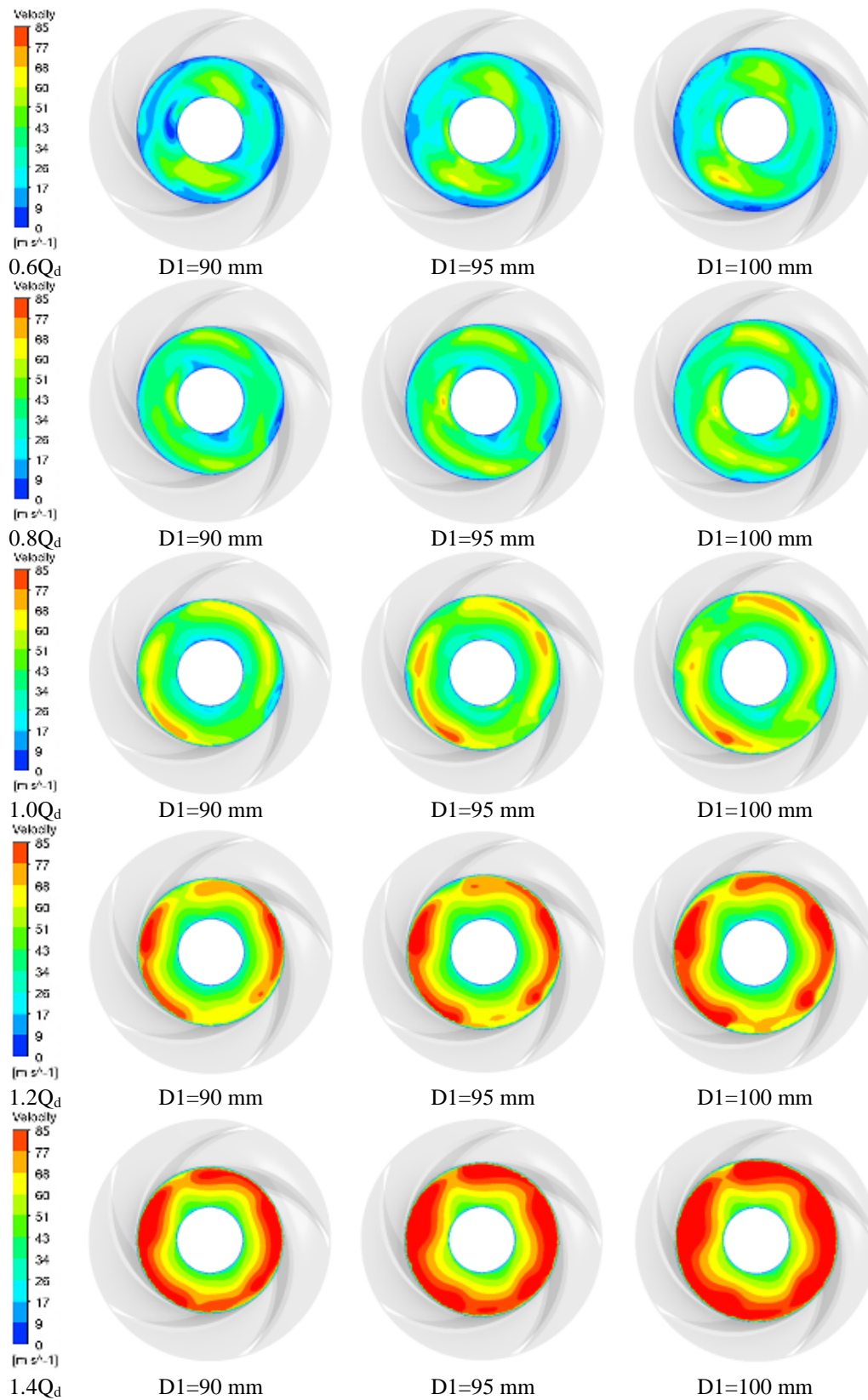**Fig. 26 The pressure distribution of impeller under different inlet diameters and working conditions**

Fig. 27 The velocity distribution of impeller inlet section under different schemes

region begins to expand. At $1.4Q_d$, the local low-pressure region distribution becomes more pronounced. This indicates that as flow rate rises, the propensity for impeller cavitation also increases, ultimately leading to a decline in the pump's cavitation performance.

5. 3. 2 Impeller Inlet Cross-Section Velocity Distribution

The inlet fluid morphology of the impeller significantly impacts its performance. Consequently, we conducted an analysis of the velocity distribution at the impeller inlet for different scenarios. Figure 27 illustrates

the velocity distribution at inlet section for distinct schemes under different operating conditions. The graphs reveal that the distribution and variation trend of the velocity at the inlet section of the impellers remain largely consistent across different operating conditions for the various schemes.

Between $0.6Q_d$ and $0.8Q_d$, the low-velocity region is concentrated near the hub and the impeller's front cover, whereas the high-velocity region is located close to the center of the flow channel circumference. As the flow rate increases, the high-velocity region expands outward along the circumference. As the high flow rate of $1.4Q_d$, the high-velocity region forms a ring-like pattern at the outer edge of the entire flow channel.

Upon comparing the velocity distribution at the impeller inlet section among different schemes under idntical operating condition, the low-velocity region gradually diminishes, whereas the high-velocity region expands. When considering the impeller pressure distribution in Fig. 26, it becomes apparent that at the low flow rate of $0.6Q_d$, the high-velocity region corresponds to the low-pressure region at the inlet of the impeller blades. This indicates that increased fluid velocity can lead to localized pressure reduction, thereby enhancing the risk of cavitation.

Under operating conditions ranging from $0.8Q_d$ to $1.4Q_d$, the velocity distribution at the impeller inlet section is relatively uniform, particularly for schemes utilizing smaller impeller diameters. In summary, the size of the impeller inlet diameter significantly influences the fluid inflow characteristics, subsequently affecting the impeller's operational state.

5. 3. 3 Impeller Inlet Cross-Section Streamline Distribution

Figure 5. 5 illustrates the distribution of the transition section and impeller shaft streamline for different schemes. Horizontally, it compares the streamline distribution under different operating conditions for the same scheme, while along the same operating conditions, it compares the streamline distribution for different schemes. Overall, as the flow rate increases, the distribution of the transition section and impeller shaft streamline becomes smoother for different schemes, resulting in a uniform increase in flow velocity and a decrease in reversed flow vortices.

Under various operating conditions, at a low flow rate of $0.6Q_d$, a limited number of reversed flow vortices emerge at the inlet of the transition section, particularly near the shaft and the outer wall of the flow channel. These vortices become more pronounced as the impeller inlet diameter increases. Additionally, the flow velocity is relatively lower near the shaft and higher near the outer wall of the transition section, primarily due to the influence of the inducer's work. The flow streamline within the impeller passage is also disturbed. However, as the impeller inlet diameter increases, the flow condition improves, albeit marginally. When the flow rate reaches $0.8Q_d$, the flow velocity gradient at the inlet of the transition section decreases, leading to a reduction in the reversed flow phenomenon. Consequently, the flow

streamline within the impeller improves.

At the design flow rate point of $1.0Q_d$, the reverse flow vortex at the inlet of the transition section disappears, while a small amount of reverse flow vortex appears near the impeller hub at the impeller inlet. Notably, larger impeller inlet diameter, result in larger reverse flow vortices, affecting the stable operation of the impeller. As the flow rate increases to $1.2Q_d$ or $1.4Q_d$, the flow velocity at the inlet becomes more uniform, resulting in a relatively stable and smooth flow. This increase in flow velocity within the impeller is significant, and without obvious vortex formation, the flow becomes regular, leading to a basically stable impeller operation. However, there is a slight fluctuation in the flow streamline at the impeller outlet. This fluctuation becomes more pronounced with increasing impeller inlet diameter, indicating a tendency to form reverse flow vortices.

Overall, a comparative analysis of the impeller pressure distribution, across various schemes reveals that the impeller inlet diameter significantly impacts the performance of the high-speed centrifugal pump. Specifically, the best efficiency is achieved when the impeller inlet diameter is set to 90 mm. Based on these findings, it is recommended that during the design phase of the impeller, a slight reduction in the inlet diameter may be considered to enhance the pump's overall performance.

6. CONCLUSIONS

The current study employed the ANSYS CFX numerical simulation software to delve into the entire flow path of a high-speed centrifugal pump. Furthermore, a multi-parameter optimization design approach was utilized to enhance the inducer and impeller. This investigation aimed to assess the influence of the inducer blade wrap angle on the performance characteristics of both the inducer and the centrifugal pump, along with the impact of the impeller inlet diameter on the hydraulic performance of the pump. Through comparative analysis, the following conclusions were drawn:

Based on the pump characteristic curve, the model pump meets the design specifications in terms of head and efficiency. Notably, the efficiency peaks at 83.46% at the design operating point. However, as the flow rate increases, the efficiency decreases rapidly.

Through the analysis of the axial section pressure field and streamline velocity field of the high-speed centrifugal pump under various operating conditions, it was observed that as the flow rate increases, the area of the low-pressure region at the inducer inlet decreases, and the pressure gradient gradually diminishes. However, a significant low-pressure region emerges at the tongue clearance. Under low flow rate conditions, due to the presence of tip clearance, a reversed flow vortex appears at the inducer inlet rim. Additionally, notable reversed flow phenomena were observed at the tongue clearance and cover clearance, which gradually dissipate as the flow rate increases. This indicates that the existence of tip clearance and tongue clearance within the pump can induce reversed flow vortices and exert a certain influence on pump performance.
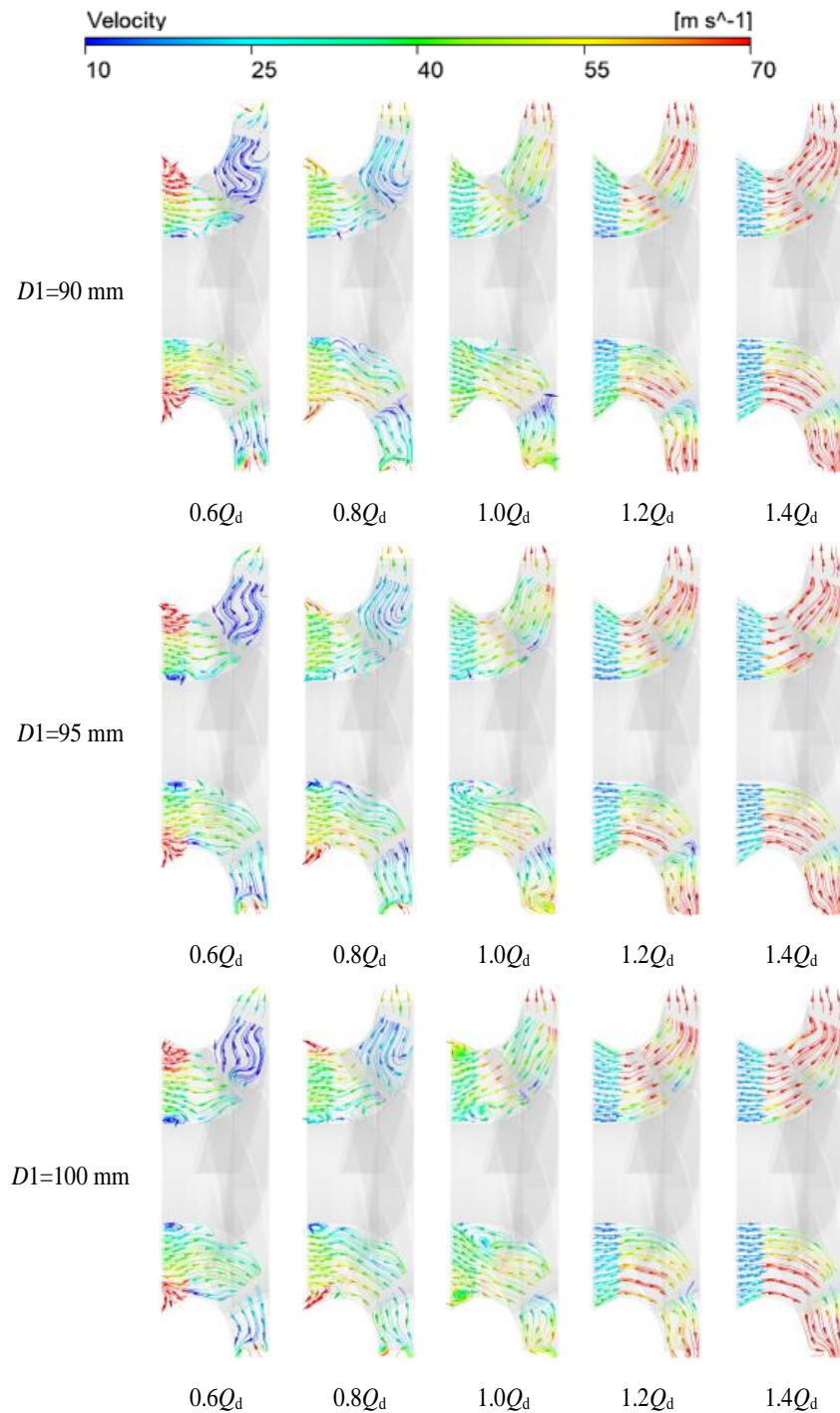
Fig. 28 The streamline distribution of transition section and impeller shaft surface under different schemes

The size of the inducer blade wrap angle has a more significant impact on the characteristics of the inducer itself compared to the external characteristics of the high-speed centrifugal pump. Specifically, a smaller blade wrap angle enables the inducer to achieve higher head and efficiency. Analyzing the pressure distribution and flow channel pressure distribution on the blade surface of the inducer reveals that both the low-pressure and high-pressure regions on the blade surface decrease as the wrap angle increases. Notably, when the blade wrap angle is $\varphi=240°$, the minimum low-pressure region occurs at the inducer inlet, resulting in the lowest cavitation probability.

Upon examining turbulence kinetic energy and streamline distribution within the impeller, it is evident that with an increase in the blade wrap angle, the turbulence kinetic energy gradually rises at both the design operating condition and large flow rate condition. This leads to greater energy dissipation. Furthermore, separation vortices emerge at the impeller inlet and volute exit, potentially affecting the normal operation of the centrifugal pump. However, when the blade wrap angle is $\varphi=240°$, the occurrence of separation vortices is reduced, optimizing the performance of the centrifugal pump. Overall, the findings suggest that an optimal blade wrap angle of $\varphi=240°$ can enhance the performance of the

centrifugal pump by minimizing cavitation probability, reducing energy dissipation, and mitigating separation vortex formation.

By examining the influence of the impeller inlet diameter on the external characteristics of the centrifugal pump, it is evident that a smaller inlet diameter leads to higher efficiency. The pressure distribution within the impeller reveals that the low-pressure region is primarily concentrated at the inlet of the impeller blades, while the high-pressure region is situated at the impeller outlet. Notably, the area of the low-pressure region expands as the inlet diameter increases. Additionally, analyzing the velocity distribution at the impeller inlet demonstrates that as the inlet diameter increases, the low-velocity region at the inlet section gradually diminishes, and the high-velocity region gradually expands. This trend elevates the cavitation probability. Observing the streamline distribution within the transition section and impeller shaft, it is observed that a smaller impeller diameter promotes a more stable fluid flow. In other words, the pump exhibits superior overall performance when the impeller inlet diameter is 90 mm. These findings suggest that a smaller impeller inlet diameter enhances pump efficiency, stabilizes fluid flow, and minimizes cavitation risk, ultimately leading to superior pump performance.

In summary, our comprehensive discussion on the centrifugal pump's external characteristics reveals a profound relationship between the impeller inlet diameter and its overall performance. A smaller inlet diameter results in higher pump efficiency, primarily due to the optimized pressure and velocity distributions within the impeller. The low-pressure region is concentrated at the inlet of the impeller blades, while the high-pressure region is situated at the outlet. As the inlet diameter decreases, the fluid flow becomes more stable, minimizing cavitation risk.

Another crucial aspect discussed is the blade wrap angle, which significantly impacts pump performance. An appropriate blade wrap angle contributes to efficient fluid redirection and pressure build-up, enhancing pump performance. This innovative insight underscores the importance of considering both inlet diameter and blade wrap angle when designing and optimizing centrifugal pumps, leading to improved overall performance and reliability.

ACKNOWLEDGEMENTS

CONFLICT OF INTEREST

We declare that we have no financial and personal relationships with other people or organizations that can inappropriately influence our work. There is no professional or other personal interest of any nature or kind in any product, service and/or company that could be construed as influencing the position presented in, or the review of, the manuscript.

AUTHORS CONTRIBUTION

Long Yun: Methodology; **Wang Rui**: Conceptualization; **Wang Haoshu**: Formal analysis & Writing - Original Draft: **He Bo**: Investigation; Fu Qiang: Project administration; **Zhu Rongsheng**: Supervision & Funding acquisition.

REFERENCES

Al-Obaidi, A. R., & Qubian, A. (2022). Effect of outlet impeller diameter on performance prediction of centrifugal pump under single-phase and cavitation flow conditions. *International Journal of Nonlinear Sciences and Numerical Simulation, 23*(7-8), 1203-1229 https://doi.org/10.1515/ijnsns-2020-0119

Cheng, X., & Zhang, A. (2020). Effect of axial matching between inducer and centrifugal pump suction chamber on cavitation performance. *Proceedings of the Institution of Mechanical Engineers, Part A: Journal of Power and Energy, 234*(7), 947-956. https://doi.org/10.1177/0957650919889506

Cheng, X., Jia, N., & Zhang, X, (2021). Effect of inducer blade dip angle on cavitation performance of high speed pump and internal energy conversion of inducer. *Journal of Xihua University 40*(2), 1-9. http://dx.doi.org/10.13465/j.cnki.jvs.2021.01.016

Cong, X., Xiao, J., Li, H., & Yang, D. (2022). Multi-objective optimization design of hydrodynamic performance of high speed centrifugal pump. *Fluid Machinery*, *50*(12), 27-34. (In Chinese). http://dx.doi.org/10.3969/j.issn.1005-0329.2022.12.005.

Cui, B. L., Zhu, K. C., Zhang, Y. L. (2019). Experimental and numerical study of the performance and cavitation flow of centrifugal pump with jetting device. *Journal of Mechanical Science and Technology, 33*(10), 4843-4853. https://doi.org/10.1007/s12206-019-0925-6

Murovec, J., Urovi, L., Novakovi, T., & Prezelj, J. (2020). Psychoacoustic approach for cavitation detection in centrifugal pumps. *Applied Acoustics, 165*, 107323.

Song, W., Shi, J., Wei, L., Hu S., Luo X., Chen J. (2020). Analysis of backflow vortex and cavitation of high-speed centrifugal pump. *Journal of Mechanical Engineering*, (04),95-103. (In Chinese). http://dx.doi.org/10.3901/JME.2020.04.095

Tong, Z. M., Xin, J. G., Tong, S. G., Yang, Z. Q., Zhao, J. Y., & Mao, J. H. (2020). Internal flow structure, fault

detection, and performance optimization of centrifugal pumps. *Journal of Zhejiang University-Science A*, (02), 85-117. https://doi.org/10.1631/jzus.A1900608

Wang, D. W., Liu, Z. L., & Zeng, J. L. (2020). Analysis of unsteady cavitation flow field and cavitation bubble characteristics for a centrifugal pump. *Fluid Mach*, *48*, 28-35. (In Chinese). http://dx.doi.org/10.3969/j.issn.1005-0329.2020.12.005.

Wang, M., Lu, J., Li, Z., Gu, F., & Chen, Z. (2023). Study on the unsteady characteristics and radial force of a single-channel centrifugal pump. *ACS Omega, 8*(2), 2291-2305. http://dx.doi.org/10.3969/j.issn.1005-0329.2020.12.005

Yang, J. J., Li, X. J., Pan, Z. Y., & He, S. (2020). Effects of cavitating flow on induced pressure fluctuation near cutwaters in double-volute centrifugal pump. *Journal of Drainage and Irrigation Machinery Engineering*, *38*(05), 445-50. (In Chinese). http://dx.doi.org/10.3969/i.issn.1674-8530.19.0011

Yu, T., Shuai, Z., Jian, J., Wang, X., Ren, K., & Dong, L., et al. (2022). Numerical study on hydrodynamic characteristics of a centrifugal pump influenced by impeller-eccentric effect. *Engineering Failure Analysis,* *138*. https://doi.org/10.1016/j.engfailanal.2022.106395

Zhang, J., Chen, X., Su, C., & Zhao, Z. (2021). Study on the influence of blade perforation near inlet edge on cavitation and turbulent kinetic energy of centrifugal pump. *Fluid Machinery*, (07),14-19+82. http://dx.doi.org/10.3969/j.issn.1005-0329.2021.07.003

Zhao, W., Kang, Y., Li, Q., & Xue, Z. (2022). Effects of different structures of blade suction surface on cavitation initiation of centrifugal pump. *Journal of Vibration and Shock,* (07), 23-30. http://dx.doi.org/10.13465/j.cnki.jvs.2022.07.003

Zhao, W., Li, Q., & Kang, Y. (2021a). Effect of suppressing cavitation of rough zone on suction surface of centrifugal pump blade. *Journal of Agricultural Machinery,* (06),169-176+214. (In Chinese). http://dx.doi.org/10.6041/j.issn.1000-1298.2021.06.017

Zhao, W., Zhu, C., Xu, Z. X., & Xu, Y. (2021b). Numerical simulation and tests for cavitation characteristics of centrifugal pump controlled by bypass device. *Journal of Vibration and Shock,* (01), 119-126. (In Chinese). https://10.13465/j.cnki.jvs.2021.01.016.